Control Engineering Practice 152 (2024) 106046

Contents lists available at ScienceDirect

Control Engineering Practice

journal homepage: www.elsevier.com/locate/conengprac

Vehicle modeling and state estimation for autonomous driving in terrain ☆

Tabish Badar [a,*], Juha Backman [a,b], Arto Visala [a]

[a] Department of Electrical Engineering and Automation, Aalto University, Maarintie 8, Espoo, 02150, Finland
[b] Farming technologies, Natural Resources Institute Finland (Luke), Lönnrotinkatu 7, Mikkeli, 50100, Finland

ARTICLE INFO

MSC:
0000
1111

Keywords:
Autonomous ground vehicles
Modeling
Simulation and experimental model validation
Observer design and state estimation
3D elevation models
Forest machines

ABSTRACT

The automobile industry usually ignores the height of the path and uses planar vehicle models to implement automatic vehicle control. In addition, existing literature mostly concerns level terrain or homogeneous road surfaces for estimating vehicle dynamics. However, ground vehicles utilized in forestry, such as forwarders, operate on uneven terrain. The vehicle models built on level terrain assumptions are inadequate to capture the rolling or pitching dynamics of such machines as rollover of such vehicles is a potential risk. Therefore, knowledge about the height profile of the path is crucial for automating such off-road operations and avoiding rollover. We propose the use of a six-degrees-of-freedom (6-DOF) dynamic vehicle model to solve the autonomous forwarder problem. An adaptive linear tire model is used in the 6-DOF model assuming the vehicle operates in a primary handling regime. The force models are modified to include the three-dimensional (3D) map information. The calibration procedures, identifying actuator dynamics, and quantifying sensor delays are also represented.

The proposed vehicle modeling contributed to realizing the continuous-discrete extended Kalman filter (CDEKF), which takes into account the 3D path during filtering and fixed-lag smoothing. Polaris (an all-terrain electric car) is used as a case study to experimentally validate the vehicle modeling and performance of the state estimator. Three types of grounds are selected — an asphalt track, a concrete track with a high elevation gradient, and a gravel track inside a forest. Stable state estimates are obtained using CDEKF and sparse 3D maps of terrains despite discontinuities in satellite navigation data inside the forest. The height estimation results are obtained with sufficient accuracy when compared to ground truth obtained by aerial 3D mapping. Finally, the proposed model's applicability for predictive control is demonstrated by utilizing the state estimates to predict future states considering (3D) terrain.

1. Introduction

The traditional Cut To Length (CLT) machine chain consists of a human-driven harvester and a human-driven forwarder as shown in Fig. 1. The harvester fells the tree, debranches, and simultaneously cuts the stem to logs in the forest. The forwarder loads and transports the logs from the forest to the roadside for transportation with trucks to wood processing mills. The heavy traditional forwarder can damage the forest ground.

We are studying a new sustainable forest machine chain: a human-driven harvester and two semiautonomous lighter forwarders without cabins and cranes. The driver of the harvester takes care of the loading of the forwarder and teleoperates at the roadside for the unloading using the crane module. One human driver can operate the new machine chain, instead of two drivers in the traditional CTL-machine chain.

The human-driven harvester is showing the spatial (2D) driving paths for the autonomous forwarders with real-time kinematic (RTK-)corrected Global Navigation Satellite Solution (GNSS) positioning in the open final cutting areas and in the thinning harvesting areas relative to trees left growing, map of trees, with LiDAR-based Forest Simultaneous Localization and Mapping (Forest SLAM) (Hyyti & Visala, 2013).

Autonomous driving is challenging in uneven forest terrain, due to e.g., slopes, stones, and stumps of harvested trees. The rollover of the forwarder is a real risk. To avoid rollover, the driving path's three-dimensional (3D) form is needed.[1] It cannot be measured with machine

☆ The research is funded by the Technology Industries of Finland Centennial Foundation and Jane and Aatos Erkko Foundation.
* Corresponding author.
E-mail address: tabish.badar@aalto.fi (T. Badar).
[1] The environment that contains a 3D representation of the path as in Badar, Ouattara, Backman, and Visala (2023) is referred to as the terrain in this article. A 2D path such as a road homogeneous road surface (Han, Choi, & Choi, 2018) will be referred to as level terrain.

https://doi.org/10.1016/j.conengprac.2024.106046
Received 4 June 2024; Received in revised form 1 August 2024; Accepted 9 August 2024
Available online 27 August 2024

Nomenclature

Subscripts

m	Refers to measured quantities
b	Refers to quantities in the body frame
e	Refers to estimated quantities
k	Refers to front-right (FR), front-left (FL), rear-right (RR), and rear-left (RL) side (tire/suspension/strut-mount point) of the vehicle
t	Refers to quantities in the tire-ground contact patch frame

Tire/Suspension/Strut

$\alpha_k, \delta_k, \gamma_k$	Sideslip angle, steering angle, and path elevation angle under kth tire (rad)
δ_c	Steering angle command (rad)
$\Delta_k, \dot{\Delta}_k$	Vertical deflection (m), and velocity of the kth spring-damper system (m/s)
$\mathcal{H}_k, \dot{\mathcal{H}}_k$	Ground truth (m), and elevation gradient (m/s)
μ_{eff}	Effective cornering stiffness coefficient
$\mathrm{C}_\alpha, \mathrm{C}_{\alpha,\text{eff}}$	initial and effective cornering stiffness (N/rad)
C_r	Coefficient of rolling resistance
B_k	Stiffness coefficient of the kth spring-damper system (N/m)
C_k	Damping coefficient of the kth spring-damper system (N s/m)
$F_{x,b}, F_{y,b}, F_{z,b}$	Longitudinal, lateral, and vertical tire forces in body frame (N)
$F_{x,t}, F_{y,t}, F_{z,t}$	Longitudinal, lateral, and vertical tire forces at tire-ground contact patch frame (N)
K, K_c	Curvature and curvature command (m^{-1})
L_k, M_k, N_k	Rolling, pitching, and yawing moment of kth strut-mount point about CG in body frame (N m)
m_k	Mass of the kth side including mass of tire (kg)
X_k, Y_k, Z_k	Longitudinal, lateral, and vertical position of kth strut-mount point in global frame (m)

Vehicle

$\dot{X}, \dot{Y}, \dot{Z}$	Longitudinal, lateral, and vertical velocities of CG in global frame (m/s)
ϕ, θ, ψ	Roll angle, pitch angle, and yaw angle (rad)
a_c	Forward acceleration command in body axes ($\mathrm{m/s}^2$)
F_x, F_y, F_z	Longitudinal, lateral, and vertical forces in body axes (N)
g	Acceleration due to gravity (9.8 $\mathrm{m/s}^2$)
I_{xx}, I_{yy}, I_{zz}	Moments of inertias about CG along longitudinal, lateral, and vertical body frame (kg m^2)
L, M, N	Rolling, pitching, and yawing moment about CG in body frame (N m)
m	mass of the vehicle (kg)
p, q, r	Roll rate, pitch rate, and yaw rate about CG in body frame (rad/s)
u, v, w	Longitudinal, lateral, and vertical velocities of CG in body frame (m/s)
X, Y, Z	Longitudinal, lateral, and vertical position of CG in global frame (m)

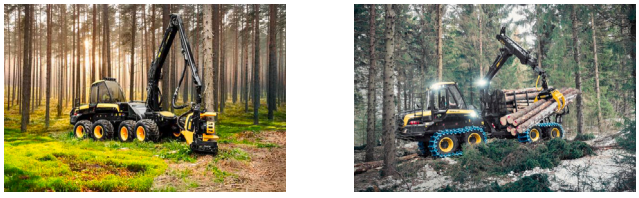

(a) Ponsse's Cobra Harvester (b) Ponsse's Bison Forwarder

Fig. 1. A harvester and a forwarder are shown, where both machines constitute the traditional CLT machine chain.
Source: Ponsse.

perception like LiDAR, because the ground is covered with snow in winter or vegetation in summer. The RTK-GNSS is inaccurate in a full forest (Badar, Ouattara, Backman, & Visala, 2024). The differential Global Positioning System (DGPS) accuracy is typically about 2-3 m, which is unsuitable even for 2D positioning. We have developed *height odometry*, reported shortly in Badar et al. (2023) and in detail in Badar et al. (2024), in which the 3D form of the solid driving path can be measured with wheel height measurements and attitude of the first going machine, for example, the harvester. The safe automatic driving along the shown paths can be implemented with Nonlinear Model Predictive Control (NMPC) of the velocity and steering. With NMPC, the 3D form of the path can be taken into account.

In this paper, the first objective is to identify a detailed nonlinear dynamic model needed in the vehicle simulators, which are then used in the initial phase development of the state estimation (Imine, Fridman, & Madani, 2012) and NMPC (Choi & Choi, 2014) in terrain. Classically, a six-degrees-of-freedom (6-DOF) dynamic model has all the forces and moments necessary to investigate the vehicle's lateral and longitudinal dynamics in detail (see, for example, Etkin and Reid (1995) and the references within). Segel (1956) introduced the famous bicycle model for automobiles by adopting a 6-DOF aerial vehicle model. His seminal work concerns analyzing the effects of a steering control mechanism on an automobile's lateral dynamics. Subsequent research has been conducted on ground vehicles that depend on incorporating or deleting elements from the 6-DOF vehicle model. Thus, each application considered in Antonov, Fehn, and Kugi (2011), Berntorp and Di Cairano (2019), Best, Gordon, and Dixon (2000), Han et al. (2018), Shim and Ghike (2007), Sun, Huang, Rudolph, and Lolenko (2015), van Aalst, Naets., Boulkroune, Nijs, and Desmet (2018), Wang and Wang (2013) and Wenzel, Burnham, Blundell, and Williams (2006) can be visualized as an extension or simplification of the 6-DOF vehicle model. Based on the results demonstrated in Berntorp (2013) and Schofield (2006), we select a 6-DOF vehicle dynamic model in this study.

In Badar, Backman and Visala (2022), a nonlinear 6-DOF dynamic model simulator for vehicles with Ackermann-type steering, Polaris electric all-terrain vehicle (e-ATV), was developed. Correspondingly, in Badar, Backman, Tariq and Visala (2022), a 6-DOF dynamic vehicle model for a center-articulated vehicle, Rakkatec, was developed using a combined center of gravity (CG) approach. A higher-order 14-DOF model from Shim and Ghike (2007) seems appealing in rollover prevention studies because it includes the dynamics of tire heights installed at each corner of the car. However, including additional dynamics

comes at a price of higher computational requirements. The vertical stiffness of bias-ply tires is very high (see, e.g., the discussion about ride comfort in Wong (2008)). Since the natural frequency of the tire modeled as an additional mass–spring system is directly proportional to the square root of the spring's coefficient of stiffness, the corresponding frequency would be very high compared to that of the suspension system. Moreover, the forest machines do not have suspension systems as in cars rather they control the instantaneous heights of the wheel using hydraulics (Badar, Backman, Tariq et al., 2022).

For the above reasons, we utilize Polaris as the case vehicle to validate vehicle modeling and state estimation.

Segel refers to CAR as a black box in his work (Segel, 1956, Figure 4). This is mainly due to a lack of precise knowledge about the tire-vehicle and tire-ground characteristics. Since then, tire modeling has become a topic of great significance for the automobile industry. In Pacejka (2012), Pacejka introduced a magic formula to model tire behavior. The formula is called magic as it suggests modeling tire forces through extensive experimentation under various loads and pressures. It does not involve first principles for its derivation. The formula depicts a linear relationship between the tire's lateral force F_y and the sideslip angle α near the origin. The constant of proportionality – in F_y versus α curve near $\alpha = 0$ – is called cornering stiffness C_α. Finding an estimate of C_α is challenging as it needs thorough experimentation, which is expensive and time-consuming (see, e.g., Georgieva and Kunchev (2015) and Vorotović, Rakicevic, Mitić, and Stamenković (2013)).

The variation of the C_α is a concern as the lateral tire forces change with tire temperature, load, and inflation pressure (Singh & Sivaramakrishnan, 2015). There exists literature that models off-road tire dynamics using semiempirical methods, e.g., Senatore and Sandu (2011). In Liang, Allen, Rosenthal, Chrstos, and Nunez (2004), for example, a tire-terrain model for vehicle simulations is considered. However, such tire-terrain interaction models are needed when it is desired to include (internal) tire parameters extensively. Such extensive off-road tire modeling was avoided in Badar, Backman, Visala (2022), where we employed Hewson's model (Hewson, 2005) to estimate C_α value using basic tire properties given in the datasheet. In this study, we extend (Badar, Backman, Visala, 2022) using an adaptation of the tire's cornering stiffness C_α through a time-varying parameter based on previous studies (Berntorp & Di Cairano, 2019; Berntorp, Quirynen, & Vaskov, 2021; Han et al., 2018; van Aalst et al., 2018). The scope of these and other lateral dynamics identification studies, such as Bascetta and Ferretti (2022), is limited to bicycle models ignoring ground elevation, roll, and pitch dynamics. A contribution here is to integrate the lateral dynamics through an effective cornering stiffness ($C_{\alpha,\text{eff}}$) to experimentally validate the 6-DOF vehicle model for autonomous driving in terrain.

The second objective is to implement the state estimation using the developed 6-DOF model and the 3D path information. The main assumption in the published results of vehicle state estimation, such as Antonov et al. (2011), Shim and Ghike (2007) and Segel (1956), has been the level terrain or homogeneous road surfaces. The vehicle state estimation can be based on inertial measurements (Berntorp & Di Cairano, 2019; van Aalst et al., 2018) to be utilized in predictive control (Berntorp et al., 2021). The focus of the automobile industry has been on road roughness classification via state estimation (González, O'brien, Li, & Cashell, 2008; Han et al., 2018). In this paper, the main distinction from Berntorp and Di Cairano (2019), Berntorp et al. (2021), Best et al. (2000), van Aalst et al. (2018) and Han et al. (2018) is that, instead of level terrain assumption, the 3D path information is utilized in the state estimation. We augment the (velocity and steering) actuator dynamics to the 6-DOF dynamic model. Both are needed to obtain state estimates to predict future states over a fixed prediction horizon.

The structure of the paper is as follows. The mathematical framework to describe the 6-DOF modeling considering a 3D path is presented in Section 2. The details about the test platforms, 3D terrain models, and state estimation methods used in this study are mentioned in Section 3. The results from calibration procedures, actuator modeling, state estimation, and model validation are provided in Section 4. The important findings of this study are discussed in Section 5. Finally, the conclusions are made in Section 6.

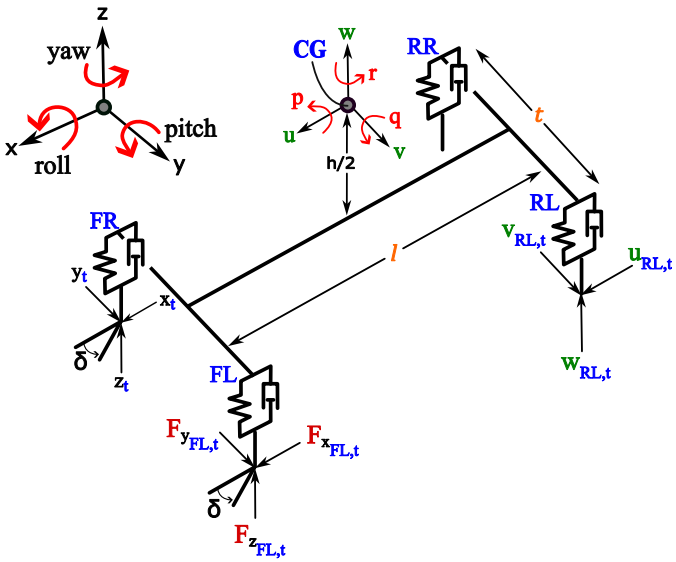

Fig. 2. Schematic of the 6-DOF car-like vehicle model is shown with a suspension at front-right (FR), front-left (FL), rear-right (RR), and rear-left (RL) corners, body-fixed (x, y, z)-frame, and FR wheel's tire-ground contact patch (x_t, y_t, z_t)-frame. The rolling, pitching, and yawing axes with positive linear velocities (u, v, w) and angular rates (p, q, r) concerning CG are also shown.

2. Models

The objective is to express the ground vehicle dynamics in the general state-space form

$$\dot{\mathbf{x}}(\tau) = \mathbf{f}\left(\mathbf{x}(\tau), \mathbf{u}(\tau), \mathbf{s}(\tau), \Theta, \tau\right) \tag{1}$$

with the (ideal) measurements described in terms of state vector as

$$\mathbf{y}(\tau) = \mathbf{g}\left(\mathbf{x}(\tau), \mathbf{s}(\tau), \Theta, \tau\right) \tag{2}$$

where $\mathbf{f}$ and $\mathbf{g}$ are the nonlinear functions that describe the dynamic and measurement models respectively, $\mathbf{x}$ is the state vector, $\mathbf{u}$ is the control input vector, $\mathbf{s}$ is the ground profile input vector and Θ constitutes internal and external 6-DOF model parameters. The state vector $\mathbf{x}$ constitutes the 3D position (X, Y, and Z) of the center of gravity (CG) in the global (or inertial) frame of reference, body velocities (u, v, and w), angular rates about CG (p, q, and r), roll angle ϕ, pitch angle θ, yaw angle ψ, and curvature K. The control input vector $\mathbf{u}$ contains curvature command K_c and forward acceleration command a_c.

The ordinary differential equations (ODEs) specifying the vehicle dynamics in terms of the state vector ($\mathbf{x}$), control input ($\mathbf{u}$), and uncontrolled ground input vector ($\mathbf{s}$) will be presented in the following sections and subsections.

2.1. Nonlinear 6-DOF vehicle model

The 6-DOF dynamical model for ground vehicles is a roll-plane model that is based on the rigid body assumption. Fig. 2 shows a 3D schematic of a car-like vehicle following the sign and coordinate transformation convention mentioned in Shim and Ghike (2007). The nomenclature of Etkin and Reid (1995) is used to describe quantities associated with the linear and angular motion of CG. The vehicle has a lumped mass m and the inertia matrix $\mathbf{I}_B$. It has a wheelbase of l, track width of t, and a total height h above the center of the rear axle (CRA).

The CG location remains fixed to the origin of (x, y, z)-frame. The system is represented by three forces – longitudinal force F_x, lateral force F_y, and vertical force F_z – along each of the body's x, y, z axes, and three moments – rolling moment L, pitching moment M, and yawing moment N – about each of the body's x, y, z axes. The linear velocities u, v, and w in Fig. 2 are the respective forward, sideways (left-side positive), and upside velocities of CG. The quantities p, q, and r represent the body angular rates about the body's x, y, and z-axes respectively. Their sign conventions concerning CG are shown by red arrows in Fig. 2.

The quantities $F_{z_{t,k}}$, $F_{y_{t,k}}$, and $F_{x_{t,k}}$ represent normal, lateral and longitudinal forces experienced by kth tire in the (x_t, y_t, z_t)-frame as shown for the FL wheel in Fig. 2. These forces are transmitted to the kth strut-mount point attached to the vehicle's body via the kth suspension system. Fig. 2 further depicts $u_{k,t}$, $v_{k,t}$, and $w_{k,t}$ for RL wheel representing the longitudinal, lateral, and vertical tire velocities respectively.

The navigation frame for the ground vehicle is the east-north-up (ENU)-frame with its X, Y, and Z-axes pointing to the east, north, and up directions respectively (Bar-Shalom, Li, & Thiagalingham, 2001). The transformation of quantities from the body-fixed coordinate frame to the global (X, Y, Z)-frame follows roll-pitch-yaw rotations. The (x_t, y_t, z_t)-frame is obtained from (x, y, z)-frame through successive roll-pitch rotations. The equations of motion (EOMs) concerning the 6-DOF vehicle are provided in the following subsections.

2.1.1. Position dynamics

The relation between inertial velocities and body velocities is given by

$$\begin{bmatrix} \dot{X} \\ \dot{Y} \\ \dot{Z} \end{bmatrix} = \mathbf{T}_1 \begin{bmatrix} u \\ v \\ w \end{bmatrix} \tag{3}$$

such that, we define

$$\mathbf{T}_1 = \underbrace{\begin{bmatrix} \cos\psi & -\sin\psi & 0 \\ \sin\psi & \cos\psi & 0 \\ 0 & 0 & 1 \end{bmatrix}}_{\mathbf{R}_z(\psi)} \underbrace{\begin{bmatrix} \cos\theta & 0 & \sin\theta \\ 0 & 1 & 0 \\ -\sin\theta & 0 & \cos\theta \end{bmatrix}}_{\mathbf{R}_y(\theta)} \underbrace{\begin{bmatrix} 1 & 0 & 0 \\ 0 & \cos\phi & -\sin\phi \\ 0 & \sin\phi & \cos\phi \end{bmatrix}}_{\mathbf{R}_x(\phi)}. \tag{4}$$

to convert quantities in the body frame to the inertial frame. Given the inertial position of CG is known, the instantaneous 3D inertial position of the center of kth wheel is given as

$$\mathbf{P}_k = \mathbf{P}_{\text{CG}} + \mathbf{T}_1 \mathbf{p}_{k,b} \tag{5}$$

where

$$\mathbf{P}_k = \begin{bmatrix} X_k \\ Y_k \\ Z_k \end{bmatrix}; \qquad \mathbf{P}_{\text{CG}} = \begin{bmatrix} X \\ Y \\ Z \end{bmatrix}; \qquad \mathbf{p}_{k,b} = \begin{bmatrix} l_k/2 \\ t_k/2 \\ h_k/2 \end{bmatrix}. \tag{6}$$

The subscript b represents the quantities concerning (x, y, z)-frame. We use the subscript k to represent the quantity associated with kth tire, strut-mount point, or corner of the vehicle. In turn, the vector $\mathbf{p}_{k,b}$ is the moment arm to compute body moments about CG concerning kth side of the vehicle. Each moment arm vector $(\mathbf{p}_{k,b})$ is defined such that after directional sign adjustments we have, e.g., $\mathbf{p}_{\text{FR},b} = \{l/2, -t/2, -h/2\}$, whereas $\mathbf{p}_{\text{RL},b} = \{-l/2, t/2, -h/2\}$.

2.1.2. Linear velocity dynamics

The EOMs describing the forward, sideways, and upward accelerations are represented as follows:

$$\begin{bmatrix} \dot{u} \\ \dot{v} \\ \dot{w} \end{bmatrix} = \frac{1}{m} \begin{bmatrix} F_x \\ F_y \\ F_z \end{bmatrix} + \mathbf{T}_1^{-1} \begin{bmatrix} 0 \\ 0 \\ -g \end{bmatrix} + \begin{bmatrix} u \\ v \\ w \end{bmatrix} \otimes \begin{bmatrix} p \\ q \\ r \end{bmatrix} \tag{7}$$

where g is the acceleration due to gravity. The operator $(\otimes)$ in Eq. (7) represents a cross product between the velocities and the rates (vector). The forces in Eq. (7) are obtained by adding all the tire forces experienced by the vehicle such that

$$F_x = \sum_k F_{x_{b,k}}, \; F_y = \sum_k F_{y_{b,k}}, \text{ and } F_z = \sum_k F_{z_{b,k}}. \tag{8}$$

2.1.3. Angular velocity dynamics

The expression of the rate of change of body rates (or the angular accelerations) is written as

$$\begin{bmatrix} \dot{p} \\ \dot{q} \\ \dot{r} \end{bmatrix} = \mathbf{I}_B^{-1} \begin{bmatrix} L - I_{xy}rp + (I_{yy} - I_{zz})qr \\ M + I_{xy}qr + (I_{zz} - I_{xx})rp \\ N + I_{xy}(p^2 - q^2) + (I_{xx} - I_{yy})pq \end{bmatrix} \tag{9}$$

Etkin and Reid (1995). The total rolling, pitching, and yawing torques or moments about CG are obtained by

$$L = \sum_k L_k, \; M = \sum_k M_k, \text{ and } N = \sum_k N_k. \tag{10}$$

The moments L_k, M_k, and N_k at the kth strut-mount point are given as

$$\begin{bmatrix} L_k \\ M_k \\ N_k \end{bmatrix} = \left(\mathbf{p}_{k,b} + \left(\mathbf{R}_z(-\psi)\mathbf{T}_1 \right)^{-1} \begin{bmatrix} 0 \\ 0 \\ -\Delta_k - h_T \end{bmatrix} \right) \otimes \begin{bmatrix} F_{x_{k,b}} \\ F_{y_{k,b}} \\ F_{z_{k,b}} \end{bmatrix} \tag{11}$$

where h_T is the tire's radius and Δ_k depicts the instantaneous vertical deflection of the kth spring of the vehicle during tire-terrain interactions. In turn, Δ_k depicts the change in length of the moment arm during compression or elongation in both car-like and articulated vehicles. It is expressed in the (x_t, y_t, z_t)-frame as highlighted in Fig. 2. Thus, $(\mathbf{R}_z(-\psi)\mathbf{T}_1)^{-1}$, which equates to $\mathbf{R}_x(-\phi)\mathbf{R}_y(-\theta)$, aligns vertical wheel displacements Δ_k to the body vector $\mathbf{p}_{k,b}$.

Finally, the relationship between the rate of change of roll, pitch, and yaw angles to the body rates is given by

$$\begin{bmatrix} \dot{\phi} \\ \dot{\theta} \\ \dot{\psi} \end{bmatrix} = \begin{bmatrix} 1 & \sin\phi\tan\theta & \cos\phi\tan\theta \\ 0 & \cos\phi & -\sin\phi \\ 0 & \sin\phi\sec\theta & \cos\phi\sec\theta \end{bmatrix} \begin{bmatrix} p \\ q \\ r \end{bmatrix}. \tag{12}$$

2.2. Modeling tire forces

In this section, we present the models describing normal, lateral, and longitudinal tire forces considering a 3D form of the path.

2.2.1. Normal force model

The purpose is to model normal tire forces when the planar (2D) ground has an instantaneous height profile. Thus, we define the load acting on the kth side as

$$F_{z_{t,k}} = -B_k(Z_k - \mathcal{H}_k) - C_k(\dot{Z}_k - \dot{\mathcal{H}}_k) \tag{13}$$

where B_k is the stiffness coefficient, C_k is the damping coefficient, Z_k is the inertial height of the kth wheel center, and $\mathcal{H}_k$ is the instantaneous height of the terrain in (X, Y, Z)-frame. Similarly, the $\dot{Z}_k$ is the vertical velocity of the center of kth wheel and $\dot{\mathcal{H}}_k$ is the rate of change of ground height. The height $\mathcal{H}_k$ is the ground truth as we assume that the *a priori* knowledge about the 3D form of the path is available utilizing (Badar et al., 2024). In turn, we specify the deterministic (though uncontrolled) input vector $\mathbf{s}(\tau) = (\mathcal{H}_k, \dot{\mathcal{H}}_k) \in \mathbb{R}^8$ in Eq. (1).

The 3D map information is given as

$$\mathbf{map}_{\text{PRI}} = \mathbf{J}\left(\left[\tilde{\text{X}}_{\text{PRI}}, \tilde{\text{Y}}_{\text{PRI}}, \tilde{\text{Z}}_{\text{PRI}} \right] \right) \tag{14}$$

where the multivariate interpolation function $\mathbf{J}(\cdot)$ incorporates all the 3D location points of the region of interest (ROI). In Eq. (14), $\tilde{\text{X}}_{\text{PRI}}$, $\tilde{\text{Y}}_{\text{PRI}}$, and $\tilde{\text{Z}}_{\text{PRI}}$ are the column vectors. Thus, the ground truth $(\mathcal{H}_k)$ and the elevation gradient $(\dot{\mathcal{H}}_k)$ are obtained from $\mathbf{map}_{\text{PRI}}$ as

$$\mathcal{H}_k = \mathbf{map}_{\text{PRI}}\left(X_k, Y_k \right) \tag{15}$$

whereas, by applying the chain rule, we get

$$\dot{\mathcal{H}}_k = \frac{\partial \mathcal{H}_k}{\partial X_k}\dot{X} + \frac{\partial \mathcal{H}_k}{\partial Y_k}\dot{Y} = \nabla \mathcal{H}_k^T \odot \mathbf{V}_{\text{ENU}}. \tag{16}$$

The expression for $\dot{\mathcal{H}}_k$ thus indicates a dot product between the (transpose of) spatial gradient of the reference height ($\nabla \mathcal{H}_k$) and the 3D inertial velocity vector ($\mathbf{V}_{\text{ENU}}$).

2.2.2. Lateral force model

The lateral tire force model is defined as

$$F_{y_{k,t}} = -\underbrace{\mu_{\text{eff}} \mathrm{C}_\alpha}_{\mathrm{C}_{\alpha,\text{eff}}} \alpha_k \tag{17}$$

where C_α is tire cornering stiffness, $\mu_{\text{eff}}(\tau) \in \mathbb{R}$ is a time-varying parameter, and α_k is lateral sideslip angle at the kth $(x_t y_t z_t)$-frame. Thus, we have

$$\alpha_k = \tan^{-1}\left(\frac{v_{k,t}}{u_{k,t}}\right) - \delta_k. \tag{18}$$

For the car-like vehicles, $\delta_{\text{RR}} = \delta_{\text{RL}} = 0$, where δ_k is the Ackermann's steering angle applied to front wheels.

The tire velocities can be obtained from CG velocities by using

$$\begin{bmatrix} u_{k,t} \\ v_{k,t} \\ w_{k,t} \end{bmatrix} = \mathbf{R}_y(\theta)\mathbf{R}_x(\phi) \begin{bmatrix} u_{k,b} \\ v_{k,b} \\ w_{k,b} \end{bmatrix} \tag{19}$$

with

$$\begin{bmatrix} u_{k,b} \\ v_{k,b} \\ w_{k,b} \end{bmatrix} = \begin{bmatrix} u \\ v \\ w \end{bmatrix} + \left(\dot{\mathbf{R}}_x(0,p) + \dot{\mathbf{R}}_y(0,q) + \dot{\mathbf{R}}_z(0,r)\right)\mathbf{p}_{k,b} \tag{20}$$

where $\dot{\mathbf{R}}_x$, $\dot{\mathbf{R}}_y$, and $\dot{\mathbf{R}}_z$ are the derivatives of the rotation matrices (Badar, Backman, Tariq et al., 2022, Appendix A).

We assume that the initial estimate of C_α is available from Badar, Backman, Visala (2022). Thus, μ_{eff} translates to what percentage of the tire's initially estimated $\mathrm{C}_\alpha(>0)$ value is effectively employed during cornering on uneven terrains. In turn, the product $\mu_{\text{eff}}\mathrm{C}_\alpha$ illustrates the effective cornering stiffness ($\mathrm{C}_{\alpha,\text{eff}}$) experienced by all the tires at each time instant. Following Ahsun, Badar, Tahir, and Aldosari (2015), van Aalst et al. (2018) and Särkkä and Svensson (2023), a simple model describing parameter dynamics is given as

$$\dot{\mu}_{\text{eff}} = 0. \tag{21}$$

2.2.3. Longitudinal force model

The tire's longitudinal force model is given as

$$F_{x_{k,t}} = F_{\mathrm{T}_{k,t}} - F_{\mathrm{R}_{k,t}} \tag{22}$$

where $F_{\mathrm{T}_{k,t}}$ is the traction force and $F_{\mathrm{R}_{k,t}}$ is the rolling resistance force (Åström & Murray, 2020). Here, we assume that the applied traction and rolling resistance forces are in the tire-ground contact patch frame (Heubaum, Münch, Costantini, Peschke, & Görges, 2022). The traction force experienced in this frame is given as

$$F_{\mathrm{T}_{k,t}} = \frac{a_c}{g} F_{z_{k,t}} \tag{23}$$

where a_c is the forward acceleration command applied to the vehicle.

The expression of the rolling resistance force is defined as

$$F_{\mathrm{R}_{k,t}} = \mathrm{C}_r \text{sgn}(u) F_{z_{k,t}} \tag{24}$$

where C_r is the coefficient of rolling friction at the tire-ground contact patch and

$$\text{sgn}(u) = \begin{cases} -1, & \text{if } u < 0, \\ 0, & \text{if } u = 0, \\ 1, & \text{if } u > 0. \end{cases} \tag{25}$$

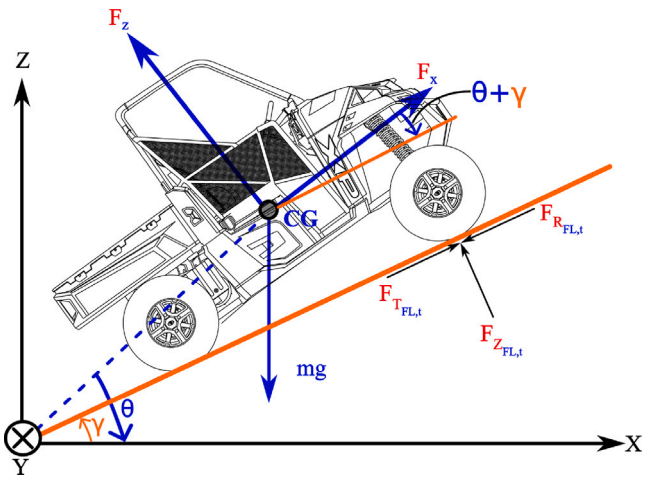

Fig. 3. Schematic displays the body forces F_x and F_z acting on the Polaris e-ATV while traveling on a path with elevation $\gamma > 0$ and pitch angle $\theta < 0$. The traction force ($F_{T_{x,t}}$), rolling resistance force ($F_{R_{x,t}}$), and normal force ($F_{z_{k,t}}$) experienced by the FL tire are also shown. The inertial (X, Y, Z)-frame is also shown where the Y-axis points into the paper.

Åström and Murray (2020). In turn, the longitudinal force experienced at the kth tire-ground contact patch becomes

$$F_{x_{k,t}} = \left(\frac{a_c}{g} - \mathrm{C}_r \text{sgn}(u)\right) F_{z_{k,t}}. \tag{26}$$

2.3. Transformation of tire forces to body forces

The tire forces expressed in the tire-ground contact patch frame are transformed into the body frame by using

$$\begin{bmatrix} F_{x_{k,b}} \\ F_{y_{k,b}} \\ F_{z_{k,b}} \end{bmatrix} = \mathbf{R}_x(-\phi)\mathbf{R}_y(-\theta)\mathbf{R}_z(\delta_k)\mathbf{R}_y(-\gamma_k) \begin{bmatrix} F_{x_{k,t}} \\ F_{y_{k,t}} \\ F_{z_{k,t}} \end{bmatrix} \tag{27}$$

where the path elevation angle γ_k is computed as

$$\gamma_k = \tan^{-1}\left(\frac{\partial \mathcal{H}_k}{\partial X}\cos\psi + \frac{\partial \mathcal{H}_k}{\partial Y}\sin\psi\right). \tag{28}$$

for kth wheel. The partial derivative terms are obtained from Eq. (16), which signify the directional gradient of ground height ($\nabla \mathcal{H}_k$) along global X and Y directions respectively. Using the cosine and sine of heading angle ψ, we align the directional gradients to the direction of wheel travel in the inertial frame of reference. Eq. (27), in turn, depicts that we first resolve the tire forces at the tire-ground contact patch for γ_k while considering a 3D path. It is followed by $\mathbf{R}_z(\delta_k)$ to transform tire forces to the motion-aligned forces (Dixon, 1996). Finally, these forces are transformed into body forces via $\mathbf{R}_x(-\phi)\mathbf{R}_y(-\theta)$ rotations.

Fig. 3 further elaborates the effect of path elevation γ_k on the kth tire forces. The forces experienced by the kth tire are resolved by the path elevation angle γ_k, whereas the body forces are resolved by $\gamma_k + \theta$ for each kth tire. In turn, it points out that the γ_k generally differs from the pitch angle θ due to suspension. In other words, the instantaneous γ_k experienced by the front tires may not equal those experienced by rear tires considering a 3D terrain.

For further analysis, we use an intermediate frame aligned with the direction of wheel travel at the tire-ground contact patch frame. In turn, the resolved tire forces are obtained as

$$\begin{bmatrix} F_{x_{k,t'}} \\ F_{y_{k,t'}} \\ F_{z_{k,t'}} \end{bmatrix} = \mathbf{R}_z(\delta_k)\mathbf{R}_y(-\gamma_k) \begin{bmatrix} F_{x_{k,t}} \\ F_{y_{k,t}} \\ F_{z_{k,t}} \end{bmatrix}. \tag{29}$$

Here, the first $\mathbf{R}_y(-\gamma_k)$ rotation aligns the z_t-axis of the tire-ground contact patch frame to the Z-axis of the global frame. The second $\mathbf{R}_z(\delta_k)$

rotation resolves the tire-aligned forces to the wheel motion-aligned forces. By expanding Eq. (29), we get

$$F_{x_{k,t}} = F_{z_{k,t}} \cos\delta_k \left(\frac{a_c}{g} \cos\gamma_k - \mathrm{C}_r \mathrm{sgn}(u) \cos\gamma_k - \sin\gamma_k \right) - F_{y_{k,t}} \sin\delta_k \quad (30)$$

where the first term is the tire traction force and the second component is the tire drag against the direction of motion due to cumulative rolling resistance force (Dixon, 1996, Chapter 2). Similarly, we have

$$F_{y_{k,t}} = F_{y_{k,t}} \cos\delta_k - F_{z_{k,t}} \sin\delta_k \left(\frac{a_c}{g} \cos\gamma_k - \mathrm{C}_r \mathrm{sgn}(u) \cos\gamma_k - \sin\gamma_k \right) \quad (31)$$

where the first term is the central force component perpendicular to the direction of motion and the second term introduces a lateral force component towards the center of rotation due to forward acceleration. Moreover, we have

$$F_{z_{k,t}} = F_{z_{k,t}} \cos\gamma_k + F_{z_{k,t}} \sin\gamma_k \left(\frac{a_c}{g} - \mathrm{C}_r \mathrm{sgn}(u) \right) \quad (32)$$

such that the first term keeps the body above ground whereas the second term is the added normal force component on kth tire in the presence of forward acceleration.

Next, we present the models for forward acceleration and steering (or curvature) inputs to the 6-DOF vehicle dynamics.

2.4. Modeling actuator dynamics

In Eq. (1), we need a model to describe the relationship between forward acceleration command a_c in Eq. (26) and the 6-DOF vehicle's forward velocity u. Similarly, a separate model must describe the relation between the steering angle δ_k in the lateral force model and the curvature input K_c applied to the (6-DOF) vehicle model. It is significant as previous studies (see, Antonov et al. (2011) and Shim and Ghike (2007)) are limited to either commercial software or manual driving of automobiles in their model validation experiments.

Fig. 3 further illustrates that given $\delta_k = 0$ and $\phi = 0$, we obtain the following expression of total longitudinal force in the body axes:

$$F_x = \sum_k F_{z_{k,t}} \left(\frac{a_c}{g} \cos(\gamma_k + \theta) - \mathrm{C}_r \mathrm{sgn}(u) \cos(\gamma_k + \theta) - \sin(\gamma_k + \theta) \right), \quad (33)$$

by first computing $F_{x,b}$ from Eq. (27) followed by utilizing $F_x = \sum_k F_{x,b}$ from Eq. (8). During the steady climb of the vehicle, we assume $\gamma_k \approx -\theta$. By using $\gamma_k \approx -\theta$ in Eq. (33) and substituting the resultant value of F_x in Eq. (7), we extract the following expression:

$$\dot{u} = a_c - g\mathrm{C}_r \mathrm{sgn}(u) + g \sin\theta. \quad (34)$$

It is equivalent to the classical cruise control model discussed in Åström and Murray (2020, Chapter 4) ignoring the aerodynamic drag considering the low-speed requirements of a forwarder. Hence, from Eq. (33), we use the following model:

$$a_c = \mathrm{C}_1 u + \mathrm{C}_2 u_c + g\mathrm{C}_r \mathrm{sgn}(u) \quad (35)$$

where C_1 and C_2 are the time constants of the first order filter to approximate $a_c \to u$ response.

Further, using a first-order ODE, we augment curvature dynamics to the 6-DOF model to describe the relation between δ_k and K_c. Hence, we write

$$\dot{K} = \mathrm{C}_3 K + \mathrm{C}_4 K_c \quad (36)$$

with

$$K_c = \frac{\tan\delta_c}{l}; \quad K = \frac{\tan\delta_k}{l} \quad (37)$$

such that coefficients C_3 and C_4 are the first-order filter coefficients. In turn, the actuator models described by Eqs. (35) and (36) are augmented to the 6-DOF vehicle dynamics to complete the continuous-time state-space representation of the system.

2.5. Modeling system for state estimation

The EOMs defined so far may still have parametric uncertainties and modeling inaccuracies. Furthermore, the sensor measurements are noisy, delayed, and received at discrete time instants. In practice, NMPC requires the *current* state to accurately predict the *future* states in an open-loop manner (see, Backman, Oksanen, and Visala (2012)). This requires fixed-lag smoothing to remove sensor and actuator delays during state estimation (Bar-Shalom et al., 2001).

Therefore, Eqs. (1)–(2) are rewritten as a *stochastic* continuous-discrete state-space model (see, e.g., Särkkä and Svensson (2023)) considering a *fixed-lag* of N intervals and modeling uncertainties to get the following *augmented* model (Moore & Tam, 1973):

$$\hat{\mathbf{x}}(\tau) = \begin{bmatrix} \dot{\tilde{\mathbf{x}}}(\tau) \\ \vdots \\ \dot{\tilde{\mathbf{x}}}_N(\tau) \end{bmatrix} = \begin{bmatrix} \mathbf{f}\left(\tilde{\mathbf{x}}(\tau), \mathbf{u}(\tau), \mathbf{s}(\tau), \tau\right) \\ \vdots \\ \mathbf{0} \end{bmatrix} + \begin{bmatrix} \Gamma(\tau) \\ \vdots \\ \mathbf{0} \end{bmatrix} \mathbf{w}(\tau) \quad (38)$$

with

$$\tilde{\mathbf{x}}(\tau) = (X, Y, Z, \phi, \theta, \psi, u, v, w, p, q, r, K, \mu_{\mathrm{eff}}) \quad (39)$$

defined as the *joint* state vector at continuous time τ, $\hat{\mathbf{x}}(\tau)$ is the *augmented* state vector, $\Gamma(\tau)$ is the dispersion matrix, and $\mathbf{w}(\tau)$ is the Brownian motion with diffusion matrix $\mathbf{Q}_c(\tau)$. Thus, the *shifted* state vector is given as

$$\begin{bmatrix} \tilde{\mathbf{x}}(\tau_{\kappa+1}) \\ \tilde{\mathbf{x}}_1(\tau_{\kappa+1}) \\ \vdots \\ \tilde{\mathbf{x}}_N(\tau_{\kappa+1}) \end{bmatrix} = \begin{bmatrix} \mathbf{I} & \mathbf{0} & \cdots & \cdots & \mathbf{0} \\ \mathbf{I} & & & & \vdots \\ \vdots & & \ddots & & \vdots \\ \mathbf{0} & & & \mathbf{I} & \mathbf{0} \end{bmatrix} \begin{bmatrix} \tilde{\mathbf{x}}(\tau_{\kappa+1} - \epsilon) \\ \tilde{\mathbf{x}}_1(\tau_{\kappa+1} - \epsilon) \\ \vdots \\ \tilde{\mathbf{x}}_N(\tau_{\kappa+1} - \epsilon) \end{bmatrix} \quad (40)$$

considering discrete measurements at $\tau_{\kappa+1}$ for arbitrarily small $\epsilon > 0$.

In turn, the *augmented* measurement model is given as

$$\mathbf{y}_\kappa = \begin{bmatrix} \mathbf{g}_1\left(\tilde{\mathbf{x}}_{N_1}(\tau_\kappa), \mathbf{s}(\tau_\kappa), \tau_\kappa\right) \\ \vdots \\ \mathbf{g}_i\left(\tilde{\mathbf{x}}_{N_i}(\tau_\kappa), \mathbf{s}(\tau_\kappa), \tau_\kappa\right) \end{bmatrix} + \mathbf{\Lambda}(\tau_\kappa)\mathbf{r}(\tau_\kappa) \quad (41)$$

such that $\mathbf{g}_i$ determines (set of) the measurement equations corresponding to ith measurements, where N_i is the delay of the ith measurements at discrete time instant τ_κ, and

$$\tilde{\mathbf{x}}_{N_i}(\tau_\kappa) = \begin{bmatrix} \mathbf{0} & \ldots & \mathbf{I} & \ldots & \mathbf{0} \end{bmatrix} \hat{\mathbf{x}}(\tau_\kappa) \quad (42)$$

where N_i specifies the number of zeros before the identity matrix in Eq. (42), $\mathbf{r}_\kappa \sim \mathcal{N}(\mathbf{0}, \mathbf{R}_\kappa)$ is the Gaussian measurement noise, and $\mathbf{\Lambda}(\tau_\kappa)$ is the noise gain matrix.

3. Research platforms, terrains and methods

The 6-DOF model and state estimation algorithm are experimentally validated using Polaris e-ATV. This section presents important details about Polaris and the reference 3D path models. Two 3D terrain models are utilized: (1) a sparse open-source 3D map, which is used for real-time state estimation algorithm, and (2) a dense UAV-based map for validation of the height estimation. We selected the continuous-discrete extended Kalman filter (CDEKF) for state estimation. We used the continuous-discrete unscented Kalman filter (CDUKF) to evaluate the performance of CDEKF.

3.1. Research platform

Fig. 4 shows the Polaris Ranger. It is 143.5 cm wide, 274.3 cm long, and 185.4 cm high above the ground. The front suspensions are MacPherson struts, while the dual A-arm suspension system is installed at the rear axle. Each of Carlisle's bias-ply tires has a rating of 25 × 9–12 with a rated tire pressure of 137.9 kPa. The (unconventional) tire sidewall's rating means that the maximum tire's (sidewall-to-sidewall)

Fig. 4. Polaris e-ATV used in this study is shown.

Fig. 5. Test tracks utilized in model validation experiments are highlighted by red markers.
Source: Google Earth.

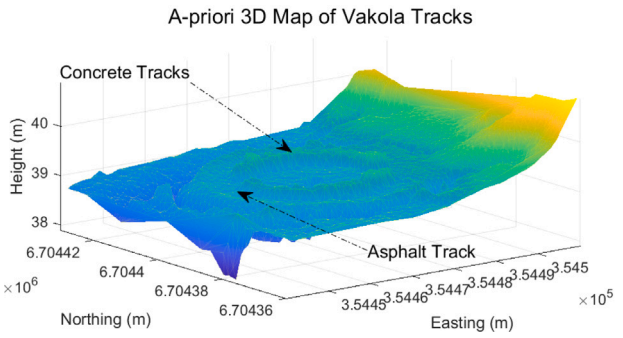

Fig. 6. The concrete tracks are semi-elliptical paths in the middle. The asphalt tracks surround these.

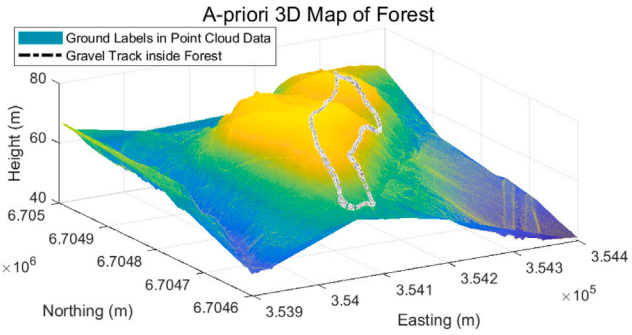

Fig. 7. The interpolated 3D point cloud data corresponding to the ground labels are used to generate $\mathbf{map}_{\text{PRI}}$ for the forest test scenario.

width is around 25 cm, and the wheel diameter is 12 inches (a wheel radius of about 15 cm) (Badar, Backman, Visala, 2022, Table 1).

The details of the important sensors and electronic control units (ECUs) installed in Polaris are presented in Badar et al. (2024). To summarize, two EPEC 5050 ECUs are used for (low-level) power steering and automatic speed control. The main computer with the Robot Operating System (ROS) receives data from each sensor and the ECUs. The main positioning sensor is the synchronous position, attitude, and navigation (SPAN) unit that combines real-time kinematic (RTK) corrections with Pinwheel's GNSS antenna and (internal) IMU data for centimetre-level positioning. The SPAN unit receives RTK corrections through a 4G data link. Four Hall-effect rotary sensors are also installed at each shaft to measure the wheels' height.

3.2. Test setup

The concrete and asphalt test tracks at Vakola, Vihti (Finland), and a gravel track in a nearby forest were selected to test state estimation. Fig. 5 depicts a satellite view of the Vakola test facility in the lower right corner, and the gravel track in the forest highlighted by a red path. The test facility at Vakola has two circular test tracks made of concrete with different elevation profiles. The concrete tracks have high elevation variations. The asphalt track encircles these concrete tracks. The asphalt track has almost a planar profile. The forest was sparse because thinning-cutting harvesting was carried out recently. Therefore, the (2D) spatial position data from the SPAN unit could be utilized in all three test scenarios as (X, Y)-positions were obtained with sufficient accuracy.

The research objectives for each test track are the following:

1. The asphalt track compares state estimation using 3D map information versus when RTK-GNSS (the exteroceptive sensor) is only used for 3D positioning.
2. The concrete tracks are used to test the vehicle modeling and state estimation when the terrain variation is high. By utilizing a dense 3D elevation map of these tracks obtained by a UAV-based system (see, Badar et al. (2023)), the online height estimation using the augmented vehicle model and sparse 3D map information is validated.
3. The forest track is used to validate state estimation using the 3D map in the presence of discontinuities in the RTK-GNSS position data. The track validates the model utilizing the 3D path information through (open-loop) state predictions over a fixed period.

3.3. A priori sparse open-source reference map

To obtain $\mathbf{map}_{\text{PRI}}$ of the regions of interest (ROIs), we use open-source 3D point cloud data provided by the National Land Survey (NLS) of Finland Maps and spatial data (2024). The 3D position data of the ROIs, as shown in Fig. 5, is in map sheet number L4124G3 of the NLS database. On average, the data has a resolution of 1.77 points/m^2 with an elevation precision of 0.15 m. The area was scanned using an airborne LiDAR system from an altitude of 2044 m in 2015. Only, the data points classified as ground labels are used to create $\mathbf{map}_{\text{PRI}}$.

Fig. 6 shows the interpolated ground points of Vakola test tracks. This dataset contains around 3000 3D location points covering a 70×70 m^2 grid. Fig. 7 shows the 3D data of the gravel road in the forest area. It consists of about 100,000 ground data points covering an area of 500×500 m^2.

The interpolation function $\mathbf{J}(\cdot)$ described in Eq. (14) can either be implemented by using the scatteredInterpolant function in MATLAB® or utilizing a multilevel B-spline interpolation method, such as proposed in Lee, Wolberg, and Shin (1997), for C++ implementation in ROS.

(a) DJI M100 Drone

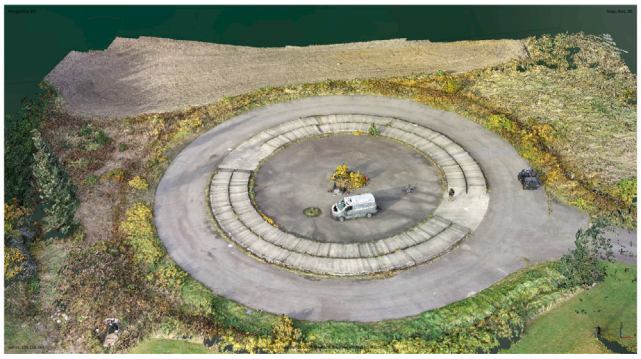

(b) 3D Model of the Test Tracks

Fig. 8. The DJI M100 drone with a machine vision camera was used to create the dense 3D map of the Vakola test tracks.

The numerical derivation of spatial gradients in Eq. (16) is obtained using the central difference method such that we define

$$\frac{\partial \mathcal{H}_k}{\partial X} = \frac{\mathbf{map}_{\mathrm{PRI}}\left(X_k + \mathrm{D}x, Y_k\right) - \mathbf{map}_{\mathrm{PRI}}\left(X_k - \mathrm{D}x, Y_k\right)}{2(\mathrm{D}x)} \tag{43}$$

with

$$\frac{\partial \mathcal{H}_k}{\partial Y} = \frac{\mathbf{map}_{\mathrm{PRI}}\left(X_k, Y_k + \mathrm{D}y\right) - \mathbf{map}_{\mathrm{PRI}}\left(X_k, Y_k - \mathrm{D}y\right)}{2(\mathrm{D}y)} \tag{44}$$

where $\mathrm{D}x$ and $\mathrm{D}y$ are the user-dependent quantities. These must be small enough to detect bumps or pits in terrain.

3.4. Dense reference map measured with UAV system

To produce the dense reference 3D model of the Vakola test tracks, a UAV equipped with a camera was used to capture overlapping images as shown in Fig. 8 (see, Badar et al. (2024) and the references within for details). These camera images are tagged with GNSS position from the onboard positioning unit. The GNSS positions are used as the initial pose of the camera by a structure from motion (SfM) and multi-view stereo matching (MVS) process which further refines the camera poses using the common features detected in different images (see Iglhaut et al. (2019) for a general presentation of the SfM-MVS photogrammetry process).

First, a sparse point cloud is built during the camera pose estimation, and then a denser point cloud is built. From the dense point cloud, a depth map is built which can be used to generate a digital elevation model of the terrain. The MetaShape software (Agisoft LLC, 2019) is used to produce the reference 3D model as shown in Fig. 8(b).

3.5. State estimation methods

A recursive Bayesian inference framework is used to compute the filtering distribution $p(\hat{\mathbf{x}}(\tau_\kappa)|\mathbf{y}_{1:\kappa})$ in an *optimal* manner (Särkkä & Svensson, 2023). The recursive computations are classically done in a standard predict and update fashion (Bar-Shalom et al., 2001). We utilize Taylor's series approximation and unscented transformation in the numerical implementation of the state estimators (Särkkä & Svensson, 2023).

3.5.1. Continuous-discrete extended Kalman filter

From an initial estimate $\hat{\mathbf{x}}(\tau_0) \sim \mathrm{N}(\mathbf{m}_0, \mathbf{P}_0)$ where $\mathbf{m}_0$ is the initial mean and $\mathbf{P}_0$ is the initial covariance, the CDEKF approximates the filtering distribution using Taylor's series expansions of the nonlinear functions $\mathbf{f}$ and $\mathbf{g}$ with respect to prior and predicted state estimates (means) respectively (see, e.g., Särkkä and Solin (2019, Algorithm 10.24)).

In the prediction step, the CDEKF propagates the mean and covariance at $\tau_{\kappa-1}$ to τ_κ by integrating the following ODEs:

$$\dot{\mathbf{m}}(\tau) = \mathbf{f}\left(\mathbf{m}(\tau), \mathbf{u}(\tau), \mathbf{s}(\tau), \tau\right) \tag{45}$$

$$\upsilon\dot{\mathbf{P}}(\tau) = \mathbf{P}(\tau)\mathbf{F}^{\mathrm{T}}_{\hat{\mathbf{x}}(\tau)}(\mathbf{m}(\tau), \tau) + \mathbf{F}_{\hat{\mathbf{x}}(\tau)}(\mathbf{m}(\tau), \tau)\mathbf{P}(\tau) + \mathbf{L}(\tau)\mathbf{Q}_c(\tau)\mathbf{L}^{\mathrm{T}}(\tau) \tag{46}$$

where $\mathbf{F}_{\hat{\mathbf{x}}}$ is the Jacobian of $\mathbf{f}$, and $\mathbf{L}(\tau) = (\Gamma(\tau), \ldots, \mathbf{0})$ is the augmented noise gain matrix in Eq. (38). For the detailed equations of update step equations in CDEKF, we refer the reader to Särkkä and Svensson (2023, Equation (10.79)).

3.5.2. Continuous-discrete unscented Kalman filter

The CDUKF has the same filtering mechanism as CDEKF. However, it uses the unscented transformations to approximate the mean and covariance as weighted combinations of sigma points. This accurately produces estimates (of mean and covariance of Gaussian random variable) to the third-order Taylor's series expansion (Wan & Van Der Merwe, 2000).

In the state prediction step, CDUKF uses the following ODEs for the mean and covariance:

$$\dot{\mathbf{m}}(\tau) = \mathbf{f}\left(\hat{\mathbf{X}}(\tau), \mathbf{u}(\tau), \mathbf{s}(\tau), \tau\right)\mathbf{w}_{\mathbf{m}} \tag{47}$$

$$\dot{\mathbf{P}}(\tau) = \mathbf{f}\left(\hat{\mathbf{X}}(\tau), \mathbf{u}(\tau), \mathbf{s}(\tau), \tau\right)\mathbf{W}\hat{\mathbf{X}}^{\mathrm{T}}(\tau) + \hat{\mathbf{X}}(\tau)\mathbf{W}\mathbf{f}^{\mathrm{T}}\left(\hat{\mathbf{X}}(\tau), \mathbf{u}(\tau), \mathbf{s}(\tau), \tau\right) + \mathbf{L}(\tau)\mathbf{Q}_c(\tau)\mathbf{L}^{\mathrm{T}}(\tau) \tag{48}$$

with the sigma point matrix given as

$$\hat{\mathbf{X}}(\tau) = \begin{bmatrix}\mathbf{m}(\tau) & \cdots & \mathbf{m}(\tau)\end{bmatrix} + \sqrt{n+\lambda}\begin{bmatrix}\mathbf{0} & \sqrt{\mathbf{P}(\tau)} & -\sqrt{\mathbf{P}(\tau)}\end{bmatrix} \tag{49}$$

where n is the dimension of $\hat{\mathbf{x}}(\tau)$, λ is a scaling parameter, and vector $\mathbf{w}_{\mathbf{m}}$ and matrix $\mathbf{W}$ defines weights (see, e.g., Särkkä (2007, Algorithm 3.1)). For the detailed set of equations at the update step in CDUKF, we refer to Särkkä (2007, Algorithm 4.6). The scaling parameter $\lambda = \eta^2(n+\beta) - n$, where η and β are the positive parameters determining the spread of sigma points (Särkkä, 2007).

3.5.3. ODE solver for state predictions

The CDEKF is implemented using the fourth-order (explicit) Runge–Kutta (RK4) method (Frogerais, Bellanger, & Senhadji, 2012; LaViola, 2003). The same numerical method is used for implementing CDUKF using (LaViola, 2003). The implementation of CDEKF using RK4 is important due to the following practical reasons:

1. Each sensor provides data to the ROS computer at $f_s = 20$ Hz. The low-level control loops operate at the same system frequency. Thus, we need state estimation at step size $h = \tau_\kappa - \tau_{\kappa-1} = 50$ ms.
2. Given $\tilde{\mathbf{x}}(\tau) \in \mathbb{R}^{14}$, the dimension of $\hat{\mathbf{x}}(\tau)$ is $(N+1)\times 14$. The maximum observed lag in sensor data was about 200 ms. At $f_s = 20$ Hz, we have $N = 4$. A higher f_s would result in increased computational load.

Table 1
Filter settings when 3D map is used.

States	**Q**-values	Measurements	**R**-values
(ϕ, θ, ψ)	$\approx 10^{-20}$	$(\phi_{\mathrm{m}}, \theta_{\mathrm{m}}, \psi_{\mathrm{m}})$	$\approx 10^{-12}$
(X, Y)	$\approx 10^{-12}$	$(X_{\mathrm{m}}, Y_{\mathrm{m}})$	$\approx 10^{-12}$
Z	$\approx 10^{-16}$	$\Delta_{k_{\mathrm{m}}}$	$\approx 10^{-10}$
(u, v, w)	$\approx 10^{-12}$	$(\mathbf{V}_{\mathrm{ENU}}, u_{\mathrm{m}})$	$\approx 10^{-10}$
K	$\approx 10^{-12}$	K_{m}	$\approx 10^{-12}$
(p, q, r)	$\approx 10^{-20}$	–	–

Table 2
Filter settings when RTK-GNSS height is used.

States	**Q**-values	Measurements	**R**-values
(ϕ, θ, ψ)	$\approx 10^{-16}$	$(\phi_{\mathrm{m}}, \theta_{\mathrm{m}}, \psi_{\mathrm{m}})$	$\approx 10^{-16}$
(X, Y)	$\approx 10^{-12}$	$(X_{\mathrm{m}}, Y_{\mathrm{m}})$	$\approx 10^{-12}$
Z	$\approx 10^{-12}$	Z_{m}	$\approx 10^{-12}$
(u, v, w)	$\approx 10^{-12}$	$(\mathbf{V}_{\mathrm{ENU}}, u_{\mathrm{m}})$	$\approx 10^{-12}$
K	$\approx 10^{-12}$	K_{m}	$\approx 10^{-12}$
(p, q, r)	$\approx 10^{-20}$	–	–

3. The explicit Euler's method requires a small h to maintain its numerical stability. The local truncation error (LTE) of the explicit Euler's method is $\mathcal{O}(h^2)$ (Ljung & Glad, 1994). A low step size is needed for state estimation as high system frequencies are expected due to high variations in wheel displacements in terrain. This naturally requires an advanced numerical approximation method. We selected RK4 as it has the LTE of $\mathcal{O}(h^5)$ based on Frogerais et al. (2012).

3.5.4. Configurations of the state estimators

We study two different configurations of the filters. The important details of these two filter configurations are given as follows:

1. In the case of 3D map, the measurement (vector) has the following form:

$$\mathbf{y}_\kappa = (X_{\mathrm{m}}, Y_{\mathrm{m}}, \phi_{\mathrm{m}}, \theta_{\mathrm{m}}, \psi_{\mathrm{m}}, V_{\mathrm{E}}, V_{\mathrm{N}}, V_{\mathrm{U}}, K_{\mathrm{m}}, u_{\mathrm{m}}, \Delta_{k_{\mathrm{m}}}) \tag{50}$$

   where the inertial 2D position in inertial frame $(X_{\mathrm{m}}, Y_{\mathrm{m}})$, roll angle ϕ_{m}, pitch angle θ_{m}, yaw (heading) angle ψ_{m}, east velocity V_{E}, north velocity V_{N}, and up velocity V_{U} are provided by the SPAN unit at 20 Hz. Moreover, curvature K_{m}, wheel speed u_{m}, and spring deflection $\Delta_{k_{\mathrm{m}}}$ measurements are sent by (respective) ECUs to the main (ROS) computer at 20 Hz. For this case, the covariances **Q** and **R** are shown in Table 1.
2. In the case of RTK-GNSS height, the measurement vector has the following form:

$$\mathbf{y}_\kappa = (X_{\mathrm{m}}, Y_{\mathrm{m}}, Z_{\mathrm{m}}, \phi_{\mathrm{m}}, \theta_{\mathrm{m}}, \psi_{\mathrm{m}}, V_{\mathrm{E}}, V_{\mathrm{N}}, V_{\mathrm{U}}, K_{\mathrm{m}}, u_{\mathrm{m}}) \tag{51}$$

   where Z_{m} is the measured RTK-GNSS antenna height. We obtain the height of each wheel (Z_k) from antenna height using (Badar et al., 2023, Equation 1). For this case, the covariances **Q** and **R** are shown in Table 2.

The measurements acquired are related to the vehicle states according to the following relations:

$$\begin{aligned} X_m &= X; \quad Y_m = Y; \quad Z_m = Z; \\ V_{\mathrm{E}} &= \dot{X}; \quad V_{\mathrm{N}} = \dot{Y}; \quad V_{\mathrm{U}} = \dot{Z}; \\ \phi_m &= \phi; \quad \theta_m = \theta; \quad \psi_m = \psi; \\ K_m &= K; \quad u_m = u; \quad \Delta_{k_m} = Z_k - \mathcal{H}_k, \end{aligned} \tag{52}$$

where the Δ_{k_m} measurements in Table 1 are used to correct the height of CG when 3D map information is used.

Table 3
Vehicle body parameters.

Parameters	Values	Units
total mass (m)	1080	kg
wheelbase (l)	1.83	m
track-width (t)	1.160	m
antenna height above ground	1.9985	m
longitudinal antenna-to-VC offset (x_{off})	−0.4476	m
lateral antenna-to-VC offset (y_{off})	0.2800	m
vertical antenna-to-VC offset (h, h_{off})	0.8767	m
tire radius (h_T)	0.3175	m
tire width (w_T)	0.2286	m
wheel radius	0.15	m
body inertia about x-axis (I_{xx})	494.6	kg m^2
body inertia about y-axis (I_{yy})	983.7	kg m^2
body inertia about z-axis (I_{zz})	862.30	kg m^2

4. Results

Prior studies (see, Särkkä and Svensson (2023) and the references within) suggest the risk of divergence of the nonlinear Kalman filters if used for (joint) state and parameter estimation. For the test vehicle, i.e., Polaris, we therefore use system calibration to determine vector Θ. After system calibration, the $\mathrm{C}_{\alpha,\mathrm{eff}}$ and vehicle states in all three test scenarios are estimated. The model validation using state predictions is presented for the forest track case. It is important to show the accuracy of the predictions with the dynamic model for the NMPC.

4.1. System calibration

This section is subdivided into three parts to show the calibration of the vehicle body, force models, and actuator models.

4.1.1. Estimation of vehicle body parameters

Polaris-specific parameters are shown in Table 3. The optimal estimates of these parameters were obtained in Badar et al. (2023). After these parameters are estimated, we get the inertial positions $\mathbf{P}_k$ from the (reported) GNSS antenna's position using (Badar et al., 2023, Equation 1). The X_k and Y_k coordinates in $\mathbf{P}_k$ are then used in Eqs. (43) and (44), respectively, for numerical computation of spatial gradients, where we select $\mathrm{D}x = 0.15$ (wheel radius), and $\mathrm{D}y = 0.25$ (tire width) for the case study.

The xz-plane is usually assumed to be the plane of symmetry for the aerial vehicles (Ahsun et al., 2015). We extend the same assumptions to the ground vehicles. Then, the off-diagonal terms in $\mathbf{I}_B$ can be eliminated if the direction of body axes coincides with the principle axes (direction of motion) of the vehicle, as discussed in Shim and Ghike (2007). With these assumptions, $\mathbf{I}_B$ becomes a diagonal matrix. This is true for Polaris for which we have approximated that mass is equally distributed to each of the four sides including two passengers. The total mass (m) in Table 3 indeed shows the vehicle's mass with two passengers. The diagonal inertia matrix terms are therefore computed using the total length, width, and height of Polaris (mentioned in Section 3.1) assuming a rectangular box.

4.1.2. Estimation of force model parameters

Fig. 9 shows the data collected from the loading/unloading experiment carried out on (FR and RL sides) of Polaris. The data suggests a linear relationship between the vertical displacement Δ_k and the normal force F_{z_k} for the kth corner of the vehicle. Fig. 9 further describes this relationship, where the blue curve is obtained using least squares. Hence, the slope of this curve is the value of the spring stiffness coefficient (B_k). These values are reported in Table 4 for each side. The C_k values were computed from $C_k = 2\zeta\sqrt{m_k K_k}$ using $\zeta = 1$ value, where ζ is the damping ratio associated with the mass–spring-damper system's second-order ODE and m_k is the mass of kth side of the vehicle.

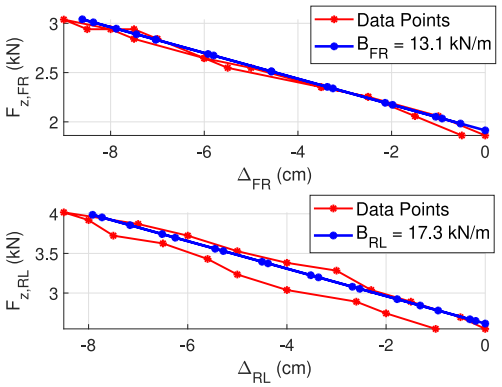

Fig. 9. The experimental data illustrating the estimation of the spring stiffness coefficient for the front right (FR) and rear left (RL) sides.

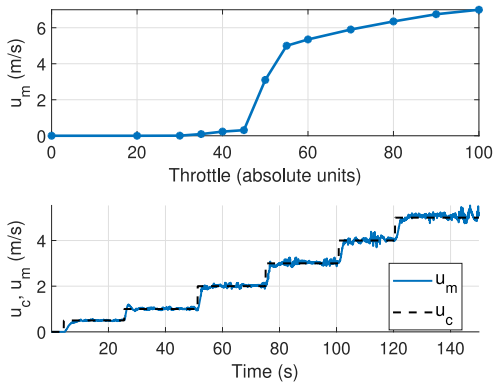

Fig. 10. The measured forward velocity (u_{m}) vs. throttle curve is identified first. The graph is used to tune the low-level velocity FF-PID controller gains.

Table 4
Suspension system parameters.

Suspension	B_k values	C_k values
Front Right (FR)	13.099 kN/m	3.762 kN/(m/s)
Front Left (FL)	15.791 kN/m	4.129 kN/(m/s)
Rear Right (RR)	16.467 kN/m	4.217 kN/(m/s)
Rear Left (RL)	17.327 kN/m	4.325 kN/(m/s)

An experiment with Polaris was carried out to estimate the rolling resistance coefficient (C_r) on an uneven (dry asphalt) road. The vehicle was driving at a constant forward velocity, about $u_c = 2.5$ m/s. Then, we set the speed command $u_c = 0$. This accounts for a velocity change of Du (of 2.5 m/s). The rolling resistance force will eventually stop the vehicle in time Dτ. Inserting $F_{T_{k,t}} = 0$ in Eq. (22) implies $a_c = 0$ in Eq. (26). Therefore, with $a_c = 0$ and $F_{z_{k,t}} = m_k g$ in Eq. (26), we get

$$m_k \frac{\mathrm{D}u}{\mathrm{D}\tau} = -\mathrm{C}_r m_k g. \tag{53}$$

From this, the magnitude of the rolling resistance coefficient is obtained as:

$$|\mathrm{C}_r| = \frac{1}{g}\frac{\mathrm{D}u}{\mathrm{D}\tau}. \tag{54}$$

This resulted in $\mathrm{C}_r = 0.0397$ from experimental data.

Using Hewson's model (Hewson, 2005), we find an initial estimate of cornering stiffness $\mathrm{C}_\alpha = 10.419$ kN/rad for the tires installed in Polaris. We restrict $|\alpha_k| \leq 10°$ considering Polaris's turn radius (r_t) does not exceed 10 m. It shows that in the primary handling regime, the Ackermann's steering angle is given by $\tan^{-1}(l/r_t)$ is $-10° \leq \delta_c \leq 10°$ (Dixon, 1988).

4.1.3. Identifying actuator models

The measured forward velocity of Polaris over the full range of throttle was first obtained from the ECU in an open-loop manner. It is shown in the upper part of Fig. 10. A feed-forward proportional–integral–derivative (FF-PID) was implemented for the (low-level) velocity controller. The resulting closed-loop $u_c \to u_m$ response is shown in the lower part of Fig. 10, where u_{m} are the speed measurements from wheel encoders sent by the ECU to ROS computer over CAN-bus.

Using another set of (closed-loop) $u_c \to u_m$ data over a velocity range of 0 to 2 m/s, the following transfer function was identified using MATLAB's TFEST command:

$$\frac{u_m(s)}{u_c(s)} = e^{(-0.2s)}\frac{1.017}{s+1.011}. \tag{55}$$

By comparing the coefficient with those mentioned in Eq. (35), we get $\mathrm{C}_1 = -1.011$ and $\mathrm{C}_2 = 1.017$. For another dataset, the a_c commands were obtained from Eq. (35) using the estimated parameter values via emulation. The computed a_c values were applied to the 6-DOF dynamic model simulator. Fig. 11 shows $a_c \to u$ model identification results such that u is the vehicle dynamic model simulator's output. However, we did not utilize the 3D path information (ground elevation, etc.) or the recorded vehicle attitude information to acquire these results.

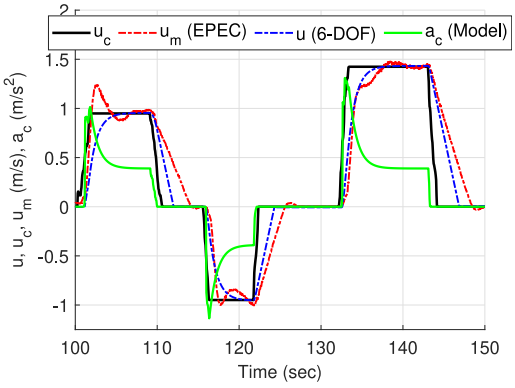

Fig. 11. The forward acceleration model identification results are shown.

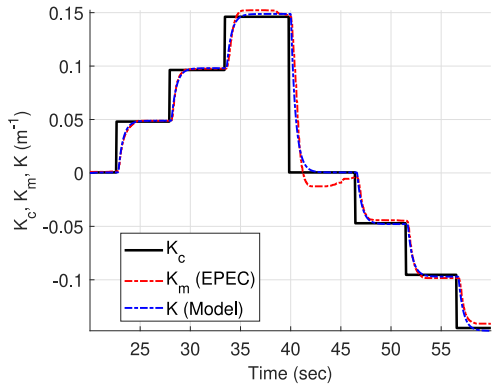

Fig. 12. Curvature model identification results are shown.

Similarly, a set of closed-loop steering (input–output) data was used to identify the coefficients of first-order steering dynamics with delay, given as

$$\frac{\delta_m(s)}{\delta_c(s)} = e^{(-0.2\ \mathrm{s})}\frac{2.165}{s+2.128} \tag{56}$$

which depicts that the (transport) delay in the steering control is about 200 ms. Thus, by comparing the coefficients of Eqs. (56) to (36), we get $\mathrm{C}_3 = -2.128$ and $\mathrm{C}_4 = 2.165$. Further using Eq. (37), the results of the curvature model identification using a separate set of steering

input–output data are depicted in Fig. 12. From the transfer function identified in Eqs. (55) and (56), we obtain the actuation delay of 200 ms. It corresponds to $N = 4$ for fixed-lag smoothing.

4.2. Online state estimation

Figs. 13, 14, and 15 summarize the state estimation results. The estimated spatial positions in Figs. 13(a), 14(a), and 15(a) are shown in the local ENU frame, however, the height data is shown in the above mean-sea-level (MSL). For brevity, only data concerning the position and height measurements from SPAN (red), the estimated position and height of the vehicle's CG (blue), and the FR wheel (dotted black) in the inertial frame of reference are shown. The FR wheel height is obtained from Eq. (5). For the forest track case, the estimated RL wheel height and inertial positions are also shown. The SPAN's height corresponds to that of the GNSS antenna height installed in Polaris e-ATV.

The flatness of the asphalt track can be noticed in Fig. 13(a), whereas high variations in the height profile of the concrete track can be seen in Fig. 14(a). Fig. 15(a) further illustrates that the height profile of the path significantly changes inside the forest, and shows the instances where height measurements had (jump) discontinuities.

Figs. 13(b), 14(b), and 15(b) show the estimation of roll (ϕ), pitch angle (θ), and yaw angle (ψ) along with body rates (p, q, and r). The estimated quantities are shown in blue whereas the measured quantities are in red.

Figs. 13(c), 14(c), and 15(c) describe the forward velocity dynamics for each experiment. The acceleration command a_c (shown in green) in each case is computed from Eq. (35) using the coefficients found in Section 4.1.3. The speed command u_c (black) in each experiment was applied via the main computer and sent to the ECU. The ECU sends the measured speed from the wheel encoders u_m (shown in red) to the main computer. CDEKF computes the estimated velocity u (shown in blue).

Figs. 13(d), 14(d), and 15(d) illustrate the estimation of the lateral force model parameters. The commanded (δ_{FR_c}) and estimated (δ_{FR}) steering angles for the front-right (FR) wheel are also shown in red and blue respectively. The predicted sideslip angle (α_{FR}) computed from Eq. (18) are also shown. To get α_{FR}, we used the estimated quantities in Eq. (18).

Fig. 16 shows the CDEKF results when RTK-GNSS height, i.e., when the measurement vector given by Eq. (51) and filter configuration mentioned in Table 2 are used. In this filter configuration, CDEKF produces smoother body rates (p, q, r) as the height profile of the path is neglected in this case. The body rates reported by SPAN remain noisier in comparison to the estimated rates (in blue) in each test. Fig. 16(b) also shows the lateral acceleration computed as $a_s = ur$.

CDEKF with RTK-GNSS height measurements for the forest track case, however, did not result in stable estimation. It is mainly due to discontinuities in height measurements illustrated in Fig. 15(a).

4.3. Model validation

The augmented system model described by Eq. (1) was simulated for fixed speed and curvature commands. This simulated a scenario where states were propagated in time using the augmented 6-DOF dynamic model without filtering. This was carried out for the period during which the u_m followed u_c closely. Thus, starting from the state estimates at $\tau = 80$ s, the system model was numerically computed using RK4 using $u_c = 1.5$ m/s for time $80 \leq \tau < 90$ s. The corresponding results are shown in Fig. 17.

In Fig. 18, the state prediction results are shown for time $200 \leq \tau < 210$ s. During this period, $u_c = 0.5$ m/s was set for Polaris. The predictions were computed for this time to validate the 6-DOF model utilizing 3D path information when the RTK-GNSS position measurements had jump discontinuities.

The CDUKF algorithm is a suitable alternative to CDEKF for model validation as it does not involve linearizations and Jacobian computations (Särkkä, 2007; Särkkä & Solin, 2019). Moreover, CDUKF is a

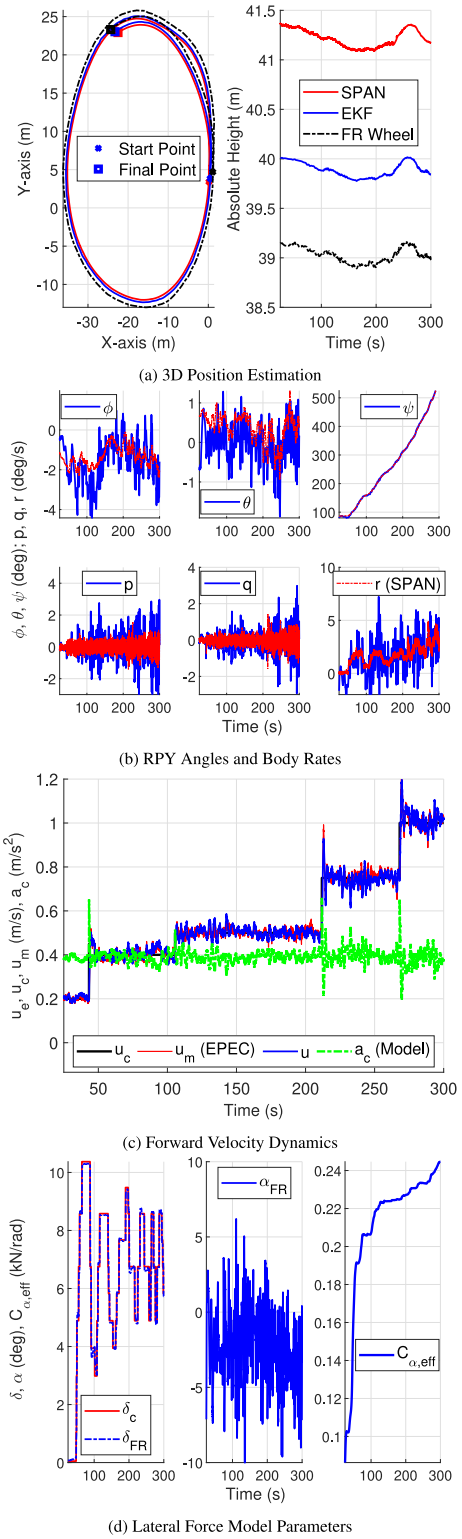

Fig. 13. Asphalt track: State estimation results using 3D map. (For interpretation of the references to color in this figure legend, the reader is referred to the web version of this article.)

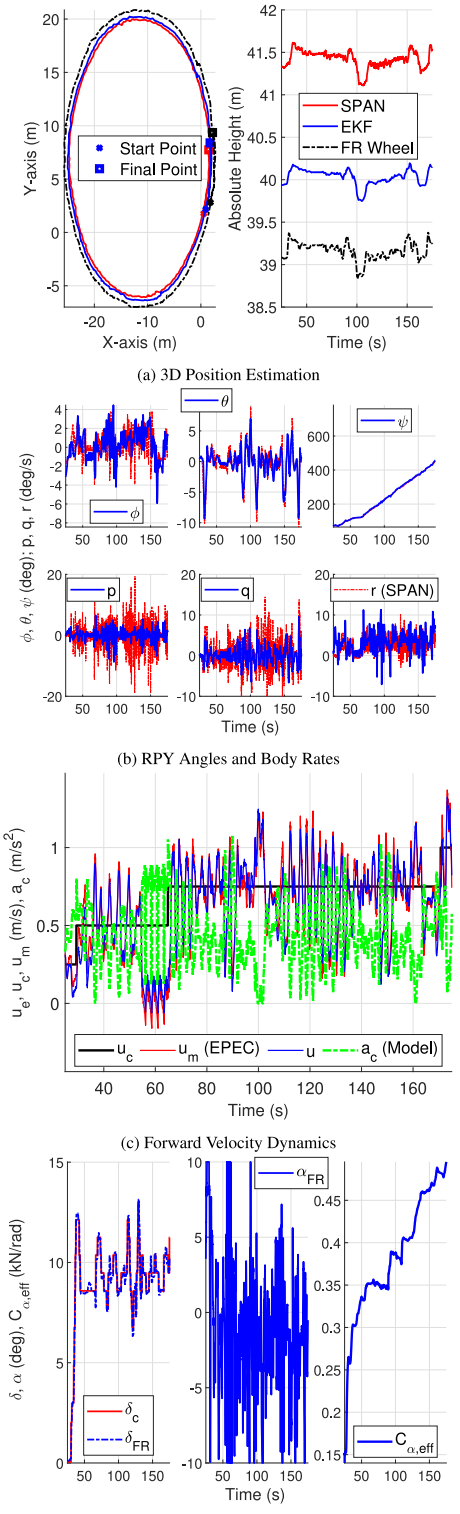

Fig. 14. Concrete track: State estimation results using 3D map. (For interpretation of the references to color in this figure legend, the reader is referred to the web version of this article.)

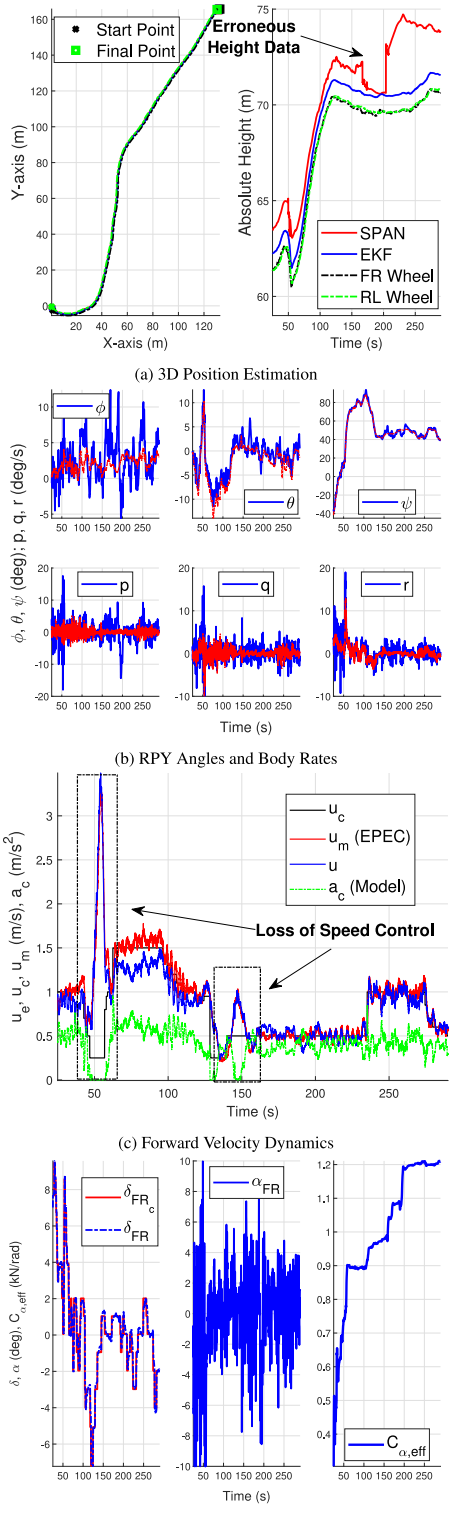

Fig. 15. Forest track: State estimation results using the 3D map. (For interpretation of the references to color in this figure legend, the reader is referred to the web version of this article.)

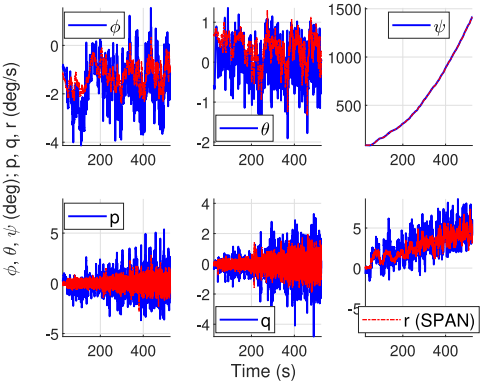

(a) RPY Angles and Body Rates

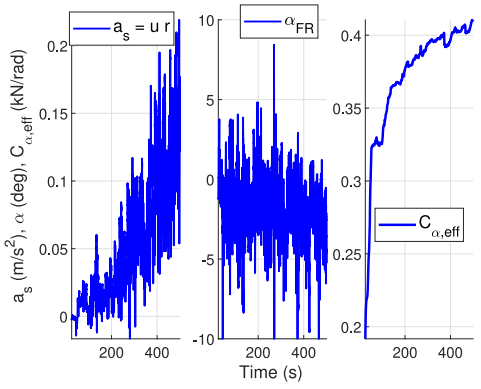

(b) Lateral Force Model Parameters

Fig. 16. Asphalt track: CDEKF results obtained using RTK-GNSS 3D positioning.

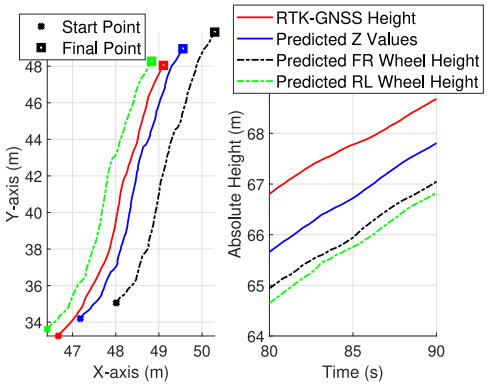

(a) Prediction of 3D Position

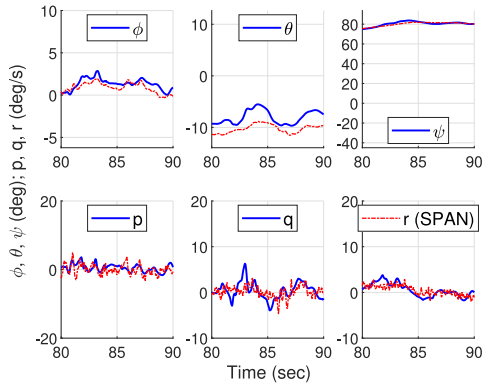

(b) Prediction of Angles and Rates

Fig. 17. Forest track: Open-loop state prediction results (shown in blue and black) are compared when SPAN measurements (shown in red) are accurate. (For interpretation of the references to color in this figure legend, the reader is referred to the web version of this article.)

preferable choice in the initial model validation phase as it is less affected by historical evidence and relies more on current observations (Yang, Shi, & Chen, 2017). Fig. 19 summarizes the important results for the forest track case when CDUKF is employed with $\eta = 0.05$ and $\beta = 0$.

5. Discussion

The important points to discuss are mentioned as follows:

1. Fig. 20 shows a zoomed-in perspective of the estimated angles and rates shown in Fig. 14(b) for the concrete track case. The CDEKF produces (ϕ, θ, ψ) estimates removing the lag. The heading (ψ) angle measured from SPAN has more delays than the roll and pitch measurements. The estimated quantities are in blue whereas the measured are in (dashed) red.
2. Fig. 21 shows the auto-correlation of measurement residuals corresponding to the (online) CDEKF and (offline) CDUKF position and velocity estimates for the forest track case. The magnitudes at non-zero lags in the auto-correlation graphs for both cases are substantially lower thus validating the CDEKF performance. Fig. 19 shows that CDEKF performance is comparable to CDUKF.
3. Fig. 22 shows the variations in the measured normal forces of the front wheels (left graph) and the right side of the vehicle (right graph). Each load value is obtained such that the change $\Delta F_{z_{k,\mathrm{m}}} = -B_k(\Delta_{z_{k,\mathrm{m}}} - \Delta_{z_{k,\mathrm{m},0}})$ is computed using B_k from Table 4, whereas $\Delta_{z_{k,\mathrm{m}}}$ is measured spring deflection and $\Delta_{z_{k,\mathrm{m},0}}$ is initial deflection at the start of test. Thus, the large fluctuations in estimated ϕ and θ on the forest track are due to high tire load variations. Such high load variations are the main cause of filter instability if a standard (discrete-discrete) EKF is used given $h = 50$ ms.
4. For validation of height estimation, we use the reference 3D map described in Section 3.4. First, we import each wheel's 2D paths into the MetaShape software. For each of the estimated 2D paths, the MetaShape exports the ground truth, i.e., the reference height of the path. Fig. 23 shows the comparison of height estimation $(Z_{k,\mathrm{EKF}})$ with the ground truth $(Z_{k,\mathrm{UAV}})$ obtained for the front wheels using UAV-based 3D mapping. The root-mean-squared errors between estimated and ground truth corresponding to the RL, FR, FL, and RR wheels are 4.4961 cm, 4.4377 cm, 4.6936 cm, and 4.3256 cm, respectively.
5. Fig. 17(a) shows that the SPAN positioning was fairly precise from 80 to 90 s. However, from 200 to 210 s, the (3D) position data provided by SPAN had several jumps as shown in Fig. 18(a). The jump in the spatial distance at around 204 s was about 0.45 m. The discontinuity in height data was about 2.5 m, which is the main cause of instability when the filter configuration mentioned in Table 2 is used. Fig. 18, thus, shows that the open-loop state predictions would not be affected by the jumps in the RTK-GNSS height data.
6. On the concrete tracks, the oscillations in u and a_c at around 55 s were due to low speed command $u_c = 0.5$ m/s. It was insufficient to accelerate Polaris forward on that part of the track. Fig. 15(c) depicts another case when Polaris experienced a loss of speed control inside the forest. However, these are problems specific to Polaris (low-level) velocity control. Moreover, tuning the FF-PID, provided the (open-loop) throttle response in Fig. 10, is not straightforward. Figs. 13(c), 14(c), and 15(c) show that state estimation was carried out despite such shortcomings specific to the test vehicle.

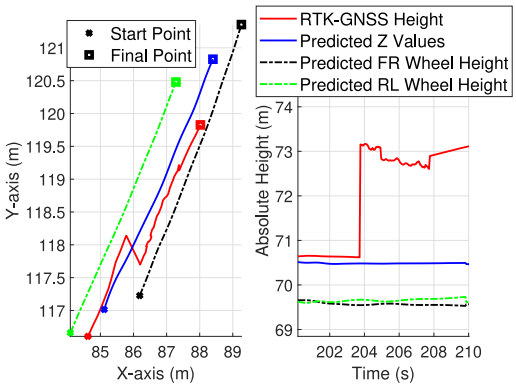

(a) Prediction of 3D Position

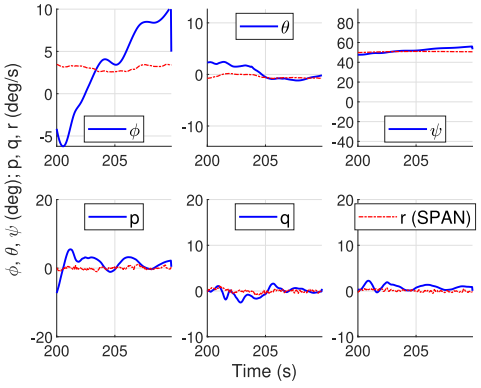

(b) Prediction of Angles and Rates

Fig. 18. Forest track: Open-loop state prediction results are compared when RTK-GNSS position data contained jump discontinuities.

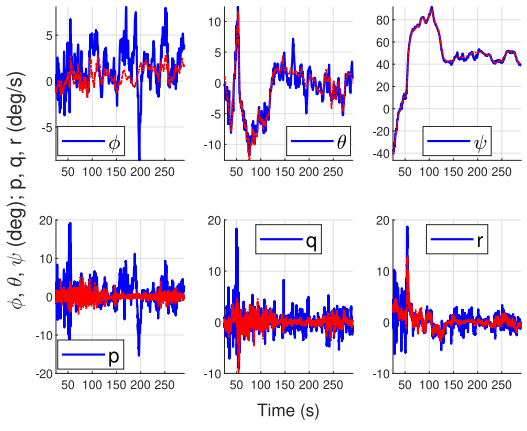

(a) RPY Angles and Body Rates

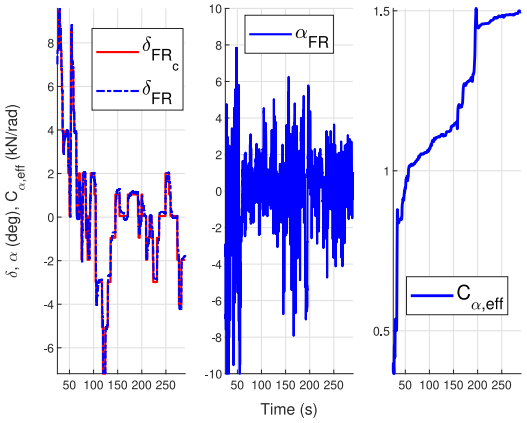

(b) Lateral Force Model Parameters

Fig. 19. Forest track: Main results when CDUKF is used.

A higher-order velocity control model may be used in Eq. (35). Here, a higher number of states to represent $a_c \rightarrow u$ model was avoided for computational reasons. Nevertheless, it does not affect the modeling aspects of this study. A contribution rather is to show that the vehicle cruise model discussed in Åström and Murray (2020) is embedded within the mathematical framework of the 6-DOF vehicle model when a 3D path is considered for describing tire forces.

7. The results in the current literature e.g., Han et al. (2018, Section II), Berntorp and Di Cairano (2019, Section VII), and Berntorp et al. (2021, Section V) show that $C_{\alpha,\text{eff}}$ converges only when the vehicle is driven at a constant velocity assuming single-track model and level terrain (homogeneous road) conditions.
   Fig. 13(d) shows $C_{\alpha,\text{eff}}$ convergence on the circular asphalt track when Polaris is driven at $u_c = 0.75$ m/s between 100 to 200 s. On the concrete track, $C_{\alpha,\text{eff}}$ continuously adapts to the changing terrain and vehicle speeds as shown in Fig. 14(d). In the forest, Fig. 15(d) also indicates a steady $C_{\alpha,\text{eff}} = 0.9$ kN/rad at $u_c = 1.5$ m/s during $60 \leq \tau \leq 100$ s and a mean value of 1.2 kN/rad during $200 \leq \tau \leq 275$ s.
   For the forest track experiment, Fig. 19(b) shows that $C_{\alpha,\text{eff}} = 1.5$ kN/rad for $200 \leq \tau \leq 275$ s. Both, the velocity and the terrain change during $200 \leq \tau \leq 275$ s, the $C_{\alpha,\text{eff}}$ however remains steady due to low steering angle ($-4° \leq \delta_c \leq 2°$) applied during this period.
   On the circular asphalt and concrete test tracks, instantaneous height variations resulted in large sideslip angles (over $\pm 10°$) as the instantaneous δ_{FR_e} were about 11° and 13.5° respectively. This is shown, respectively, in Figs. 13(d) and 14(d). Fig. 15(d) also shows large α_{FR} values in the forest at the start of the test when high δ_{FR_c} was sent while the Polaris lost speed control. These instances depict a nonlinear tire behavior. With further analysis using Fig. 16(b), we noticed that CDEKF also depends on the forward velocity (u), and yaw rate (r) to adapt lateral vehicle dynamics.
   The contribution of the study is to show that the estimation of vehicle dynamics considering 3D paths can be achieved by utilizing a (simple) linear lateral tire force model at the desired system frequency. The inclusion of a complex nonlinear tire model, such as Fiala or Pacejka (see, Bascetta and Ferretti (2022) and references within), in the 6-DOF vehicle dynamic model would be straightforward provided extensive tire parameterization is needed.

6. Conclusions and future work

This article has demonstrated the utilization of 3D path information in 6-DOF vehicle modeling for off-road vehicles. This contributed to the design of a nonlinear model-based state estimator in a continuous-discrete configuration considering 3D map information and fixed-lag smoothing. An adaptive lateral tire force model was used to validate the state estimator performance, where an initial estimate of C_α was obtained from Hewson's method. The numerical approximation of state predictions in CDEKF was implemented using the RK4 method. In turn, the CDEKF results were obtained in three very distinct test scenarios at

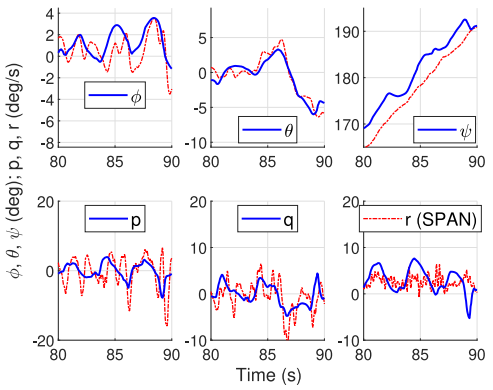

Fig. 20. Concrete track: A zoomed-in perspective of angle and body rate estimation is shown to highlight fixed-lag smoothing.

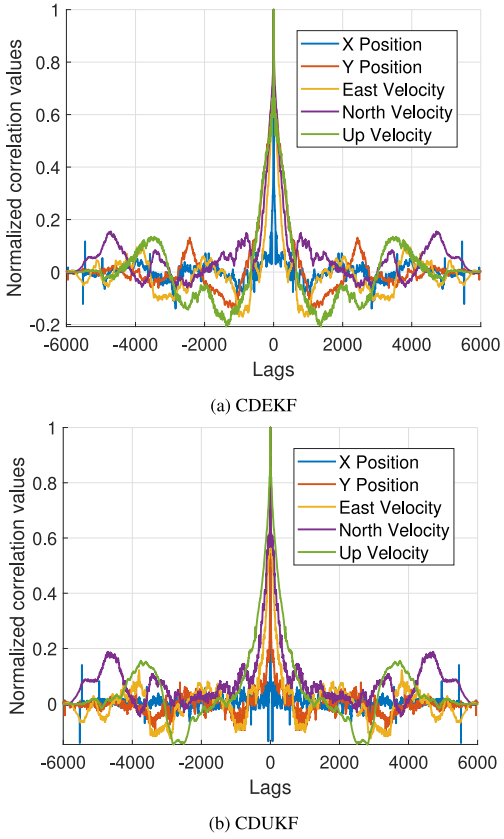

Fig. 21. Forest track: The auto-correlation of measurement residuals (innovations) obtained from CDEKF are compared with those from CDUKF.

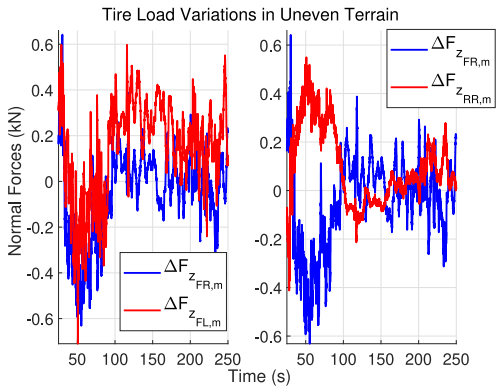

Fig. 22. Forest track: The normal force measurements with initial weight and sign adjustments. (For interpretation of the references to color in this figure legend, the reader is referred to the web version of this article.)

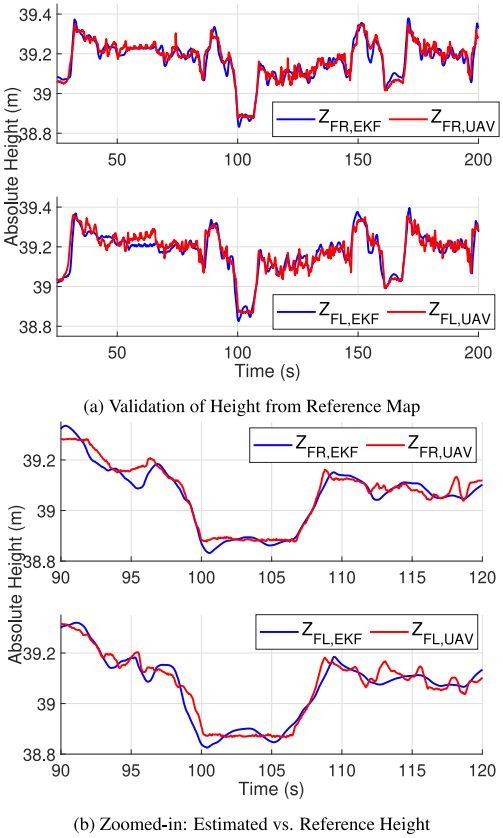

Fig. 23. Concrete track: The validation of estimated height data is done using the reference 3D model obtained by employing a UAV system.

20 Hz. Evaluation of the vehicle states and effective C_α estimation for each experiment show that the applied state estimator is reasonably robust in terms of coping with variations in tire-terrain interactions.

The main limitation of autonomous driving in terrain is addressed by estimating height using 3D path information. Utilizing a UAV-based dense 3D reference map, the accuracy of the height estimation using a sparse 3D map was demonstrated. The applicability of an augmented 6-DOF dynamic model utilizing 3D map data for the NMPC was shown via state predictions across a fixed horizon. Particularly, inside the forest, where height data from exteroceptive sensors is unreliable, predictions of 3D positions, angles, and rates were obtained. Thus, information about the 3D form of the path is needed for stable estimation and automatic vehicle operations in terrain. The data analysis further pointed out that a higher-order (e.g., 14-DOF) vehicle dynamic model would be computationally expensive in the online rollover prevention methods. On the other hand, simpler (dual or single-track) models designed assuming flat terrain (homogeneous road conditions) would be insufficient in estimating the rolling (and pitching) dynamics of the vehicle in terrain. Overall, we demonstrated that the augmented 6-DOF vehicle model and the CDEKF utilizing (sparse) 3D map information are viable solutions to the autonomous forwarder problem.

The real-time NMPC of steering and speed further requires careful tuning of the parameters considering a realistic forest terrain. A dual-(CD)EKF setup seems a suitable choice for the joint estimation of crucial parameters and vehicle states. However, these will be discussed in our future work.

CRediT authorship contribution statement

Tabish Badar: Writing – original draft, Validation, Software, Methodology, Investigation, Formal analysis, Data curation, Conceptualization. **Juha Backman:** Writing – review & editing, Visualization, Validation, Supervision, Methodology, Investigation, Conceptualization. **Arto Visala:** Writing – review & editing, Supervision, Resources, Project administration, Funding acquisition, Conceptualization.

Declaration of competing interest

The authors declare that they have no known competing financial interests or personal relationships that could have appeared to influence the work reported in this paper.

Acknowledgments

The authors acknowledge the Department of Electrical Engineering and Automation at Aalto University for making this research possible. Special thanks to the Technology Industries of Finland Centennial Foundation and the Jane and Aatos Erkko Foundation for providing funding for the **Autologger** project through The Future Makers initiative.

References

Agisoft LLC (2019). Agisoft metashape user manual, professional edition, version 1.5.

Ahsun, U., Badar, T., Tahir, S., & Aldosari, S. (2015). Real-time identification of propeller-engine parameters for fixed wing UAVs. *IFAC-PapersOnLine*, *48*(28), 1082–1087, 17th IFAC Symposium on System Identification SYSID 2015.

Antonov, S., Fehn, A., & Kugi, A. (2011). Unscented Kalman filter for vehicle state estimation. *Vehicle System Dynamics*, *49*(9), 1497–1520.

Åström, K. J., & Murray, R. M. (2020). *Feedback systems: An introduction for scientists and engineers* (2nd ed.). Princeton University Press.

Backman, J., Oksanen, T., & Visala, A. (2012). Navigation system for agricultural machines: Nonlinear model predictive path tracking. *Computers and Electronics in Agriculture*, *82*, 32–43.

Badar, T., Backman, J., Tariq, U., & Visala, A. (2022). Nonlinear 6-DOF dynamic simulations for center-articulated vehicles with combined CG. *IFAC-PapersOnLine*, *55*(14), 95–100, 11th IFAC Symposium on Intelligent Autonomous Vehicles IAV 2022.

Badar, T., Backman, J., & Visala, A. (2022). Modeling of tire lateral forces in non-linear 6-DOF simulations for off-road vehicles. *IFAC-PapersOnLine*, *55*(32), 12–17, 7th IFAC Conference on Sensing, Control and Automation Technologies for Agriculture AGRICONTROL 2022.

Badar, T., Ouattara, I., Backman, J., & Visala, A. (2023). Estimation of 3D form of the path for autonomous driving in terrain. *IFAC-PapersOnLine*, *56*(2), 4916–4921, 22nd IFAC World Congress.

Badar, T., Ouattara, I., Backman, J., & Visala, A. (2024). Estimation of the height profile of the path for autonomous driving in terrain. *Computers and Electronics in Agriculture*, *219C*, Article 108806.

Bar-Shalom, Y., Li, X. R., & Thiagalingham, K. (2001). *Estimation with applications to tracking and navigation*. John-Wiley and Sons, Inc..

Bascetta, L., & Ferretti, G. (2022). LFT-based identification of lateral vehicle dynamics. *IEEE Transactions on Vehicular Technology*, *71*(2), 1349–1362.

Berntorp, K. (2013). *Derivation of a six degrees-of-freedom ground-vehicle model for automotive applications*: *Technical reports TFRT-7627*, Department of Automatic Control, Lund Institute of Technology, Lund University.

Berntorp, K., & Di Cairano, S. (2019). Tire-stiffness and vehicle-state estimation based on noise-adaptive particle filtering. *IEEE Transactions on Control Systems Technology*, *27*(3), 1100–1114.

Berntorp, K., Quirynen, R., & Vaskov, S. (2021). Joint tire-stiffness and vehicle-inertial parameter estimation for improved predictive control. In *2021 American control conference* (pp. 186–191).

Best, M., Gordon, T., & Dixon, P. (2000). An extended adaptive Kalman filter for real-time state estimation of vehicle handling dynamics. *Vehicle System Dynamics*, *34*(1), 57–75.

Choi, M., & Choi, S. B. (2014). Model predictive control for vehicle yaw stability with practical concerns. *IEEE Transactions on Vehicular Technology*, *63*(8), 3539–3548.

Dixon, J. C. (1988). Linear and non-linear steady state vehicle handling. *Proceedings of the Institution of Mechanical Engineers, Part D: Transport Engineering*, *202*(3), 173–186.

Dixon, J. C. (1996). *Tires, suspension and handling* (2nd ed.). USA: SAE International.

Etkin, B., & Reid, L. D. (1995). *Dynamics of flight: Stability and control* (3rd ed.). USA: John Wiley and Sons.

Frogerais, P., Bellanger, J.-J., & Senhadji, L. (2012). Various ways to compute the continuous-discrete extended Kalman filter. *IEEE Transactions on Automatic Control*, *57*(4), 1000–1004.

Georgieva, H., & Kunchev, L. (2015). Experimental determination of tyre lateral force: Application to tyre cornering stiffness. *Applied Mechanics and Materials*, *798*, 41–47.

González, A., O'brien, E., Li, Y.-Y., & Cashell, K. (2008). The use of vehicle acceleration measurements to estimate road roughness. *Vehicle System Dynamics*, *46*(6), 483–499.

Han, K., Choi, M., & Choi, S. B. (2018). Estimation of the tire cornering stiffness as a road surface classification indicator using understeering characteristics. *IEEE Transactions on Vehicular Technology*, *67*(8), 6851–6860.

Heubaum, M., Münch, P., Costantini, G., Peschke, T., & Görges, D. (2022). Slip detection and control for harvesting machines. *IFAC-PapersOnLine*, *55*(32), 18–23.

Hewson, P. (2005). Method for estimating tyre cornering stiffness from basic tyre information. *Proceedings of the Institution of Mechanical Engineers, Part D (Journal of Automobile Engineering)*, *219*(12), 1407–1412.

Hyyti, H., & Visala, A. (2013). Feature based modeling and mapping of tree trunks and natural terrain using 3D laser scanner measurement system. *IFAC Proceedings Volumes*, *46*(10), 248–255, 8th IFAC Symposium on Intelligent Autonomous Vehicles.

Iglhaut, J., Cabo, C., Puliti, S., Piermattei, L., O'Connor, J., & Rosette, J. (2019). Structure from motion photogrammetry in forestry: a review. *Current Forestry Reports*, *5*.

Imine, H., Fridman, L. M., & Madani, T. (2012). Steering control for rollover avoidance of heavy vehicles. *IEEE Transactions on Vehicular Technology*, *61*(8), 3499–3509.

LaViola, J. (2003). A comparison of unscented and extended Kalman filtering for estimating quaternion motion. *Vol. 3*, In *Proceedings of the 2003 American control conference, 2003* (pp. 2435–2440). vol.3.

Lee, S., Wolberg, G., & Shin, S. (1997). Scattered data interpolation with multilevel B-splines. *IEEE Transactions on Visualization and Computer Graphics*, *3*(3), 228–244.

Liang, C.-Y., Allen, R. W., Rosenthal, T. J., Chrstos, J. P., & Nunez, P. (2004). Tire modeling for off-road vehicle simulation. In *SAE 2004 automotive dynamics, stability & controls conference and exhibition*. SAE International.

Ljung, L., & Glad, T. (1994). *Prentice-Hall information and system science series*, *Modeling of dynamic systems*.

Maps and spatial data, National Land Survey of Finland. http://www.maanmittauslaitos.fi/en/maps-and-spatial-data.

Moore, J. B., & Tam, P. K. (1973). Fixed-lag smoothing for nonlinear systems with discrete measurements. *Information Sciences*, *6*, 151–160.

Pacejka, H. B. (2012). *Tire and vehicle dynamics* (3rd ed,). Oxford: Butterworth-Heinemann.

Särkkä, S. (2007). On unscented Kalman filtering for state estimation of continuous-time nonlinear systems. *IEEE Transactions on Automatic Control*, *52*(9), 1631–1641.

Särkkä, S., & Solin, A. (2019). *Institute of mathematical statistics textbooks*, *Applied stochastic differential equations*. Cambridge University Press.

Särkkä, S., & Svensson, L. (2023). *Institute of mathematical statistics textbooks*, *Bayesian filtering and smoothing* (2nd ed.). Cambridge University Press.

Schofield, B. (2006). *Vehicle dynamics control for rollover prevention* (Ph.D. thesis), Department of Automatic Control, Lund Institute of Technology, Lund University.

Segel, L. (1956). Theoretical prediction and experimental substantiation of the response of the automobile to steering control. *Proceedings of the Institution of Mechanical Engineers: Automobile Division*, *10*(1), 310–330.

Senatore, C., & Sandu, C. (2011). Off-road tire modeling and the multi-pass effect for vehicle dynamics simulation. *Journal of Terramechanics*, *48*(4), 265–276.

Shim, T., & Ghike, C. (2007). Understanding the limitations of different vehicle models for roll dynamics studies. *Vehicle System Dynamics*, *45*(3), 191–216.

Singh, K. B., & Sivaramakrishnan, S. (2015). An adaptive tire model for enhanced vehicle control systems. *SAE International Journal of Passenger Cars - Mechanical Systems*, *8*(1), 128–145.

Sun, F., Huang, X., Rudolph, J., & Lolenko, K. (2015). Vehicle state estimation for anti-lock control with nonlinear observer. *Control Engineering Practice*, *43*, 69–84.

van Aalst, S., Naets., F., Boulkroune, B., Nijs, W. D., & Desmet, W. (2018). An adaptive vehicle sideslip estimator for reliable estimation in low and high excitation driving. *IFAC-PapersOnLine*, *51*(9), 243–248, 15th IFAC Symposium on Control in Transportation Systems CTS 2018.

Vorotović, G., Rakicevic, B., Mitić, S., & Stamenković, D. (2013). Determination of cornering stiffness through integration of a mathematical model and real vehicle exploitation parameters. *FME Transactions*, *41*, 66–71.

Wan, E., & Van Der Merwe, R. (2000). The unscented Kalman filter for nonlinear estimation. In *Proceedings of the IEEE 2000 adaptive systems for signal processing, communications, and control symposium* (pp. 153–158).

Wang, R., & Wang, J. (2013). Tire–road friction coefficient and tire cornering stiffness estimation based on longitudinal tire force difference generation. *Control Engineering Practice*, *21*(1), 65–75.

Wenzel, T. A., Burnham, K. J., Blundell, M. V., & Williams, R. A. (2006). Dual extended Kalman filter for vehicle state and parameter estimation. *Vehicle System Dynamics*, *44*(2), 153–171.

Wong, J. Y. (2008). *Theory of ground vehicles* (4th ed.). New York, USA: John Wiley and Sons, Inc..

Yang, C., Shi, W., & Chen, W. (2017). Comparison of unscented and extended Kalman filters with application in vehicle navigation. *The Journal of Navigation*, *70*(2), 411–431.